DIPLOMARBEIT

Coincidence Electron Microscopy Studies on Coherent and Incoherent Cathodoluminescence Using Timepix3

zur Erlangung des akademischen Grades
Diplom-Ingenieur

im Rahmen des Studiums
Technische Physik

eingereicht von

Dominik Hornof

Matrikelnummer 11912043

durchgeführt am Atominstitut der Fakultät für Physik
der Technischen Universität Wien

unter der Anleitung von
Assoz. Prof. Dr. Philipp Haslinger

Wien, April 16, 2025

Dominik Hornof

Philipp Haslinger

Abstract

Microscopy is the study of objects that are too small for the naked eye. By using electrons as probe particles, scientists can explore the nanoscopic world on atomic-length scales.

When electrons interact with a material, they can induce the emission of light—a phenomenon known as cathodoluminescence (CL). This emitted light may originate either directly from the electron impact or through intermediate processes, classified as coherent or incoherent CL. A primary distinction between these mechanisms lies in the temporal delay between the electron-matter interaction and subsequent photon emission. Additionally, the underlying excitation processes may be distinguished by detecting electron-photon coincidences using advanced time-resolved sensor technology, such as detectors capable of registering single-particle events with nanosecond precision.

In this Master's thesis, a coincidence measurement setup using a Timepix3 camera and single-photon counting modules is presented in a transmission electron microscope (TEM). A statistical evaluation method for analysing time differences between electron-photon pairs is introduced to reveal and interpret temporal correlations. Finally, the experimental setup is tested on a silicon membrane and a micro-diamond containing silicon vacancy centres to study electron-photon correlations in coherent and incoherent cathodoluminescence.

"The paradox consists, loosely speaking, in the fact that probability theory is able to predict with uncanny precision the overall outcome of processes made up out of a large number of individual happenings, each of which in itself is unpredictable. In other words, we observe a large number of uncertainties producing a certainty, a large number of chance events creating a lawful total outcome. But, paradoxical or not, it works."
(Arthur Koestler, 1972, *The Roots of Coincidence*)

Contents

1 Introduction

"What a coincidence!"-a phrase that comes to mind when meeting someone unexpectedly in a random place. In experimental physics, the term "coincidence" has a far more specific implication. It refers to the detection of signals within defined time windows. This concept can be found in many fields of research, from probing nuclear decay processes [1] to investigating quantum entanglement [2]. By tagging the time stamps and counting the number of coincidences, we can determine whether their detection events are correlated or just a random coincidence. Furthermore, analysing the correlations can shine light on the underlying processes that give rise to the observed coincidences.

One new research area which benefits from this concept is electron microscopy. As electrons interact with matter, they can cause the emission of a photon in a process called "cathodoluminescence" (CL). This term summarises a variety of possibilities for how an electron impact leads to a photon, either directly or indirectly. By measuring temporal correlations between electrons and photons, we gain insights into which CL processes dominate in the specimen. This information not only advances our existing knowledge of electron-photon interactions, but also allows us to develop novel analytical methods [3] and design sensitive measurements to increase image quality at low dose rates [4]. Such improvements are crucial for the investigation of fragile specimens and the advancement of high-resolution imaging. This Master's thesis presents an experimental setup for detecting electron-photon coincidences within a transmission electron microscope (TEM). By synchronising a Timepix3 (TP3) camera with a single-photon detector, we want to study the fundamental mechanisms underlying electron-photon interactions and their temporal correlations.

We begin in Ch. 2 with an introduction of wave phenomena and temporal correlations in cathodoluminescence. Next, we learn about the components of a TEM and the experimental setup for coincidence electron microscopy in Ch. 3. Ch. 4 describes a calibration routine, as well as a novel method for evaluating the temporal consistency of electron events recorded by the Timepix3 camera. We investigate electron-photon correlations in coherent CL that arise from a detectable electron recoil associated with the emission of a photon in Ch. 5. Ch. 6 addresses the challenges of detecting incoherent CL signals from silicon vacancy centres within micro-diamonds. Finally, Ch. 7 discusses the key findings of coincidence electron microscopy, as well as its future applications.

2 Fundamental concepts

Electron microscopy combines many concepts from classical and quantum physics. Geometric optics, a classic model that describes light propagation in terms of rays, is still used today to elaborate the foundation of image formation under a microscope. In 1881, Ernst Abbe discovered that the fundamental limit of point resolution in a microscope is mainly determined by the wavelength of the illumination source [5]. Ernst Ruska and Max Knoll [6] realised a solution to overcome the optical resolution limits by using electrons instead of light. In recent years, point resolution below 50 pm has been observed in advanced electron microscopic imaging techniques [7].

This chapter covers topics about characteristic wave phenomena, the electron as a matter-wave, and temporal correlations in cathodoluminescence. For in-depth explanations about electron microscopy, I refer to the book "Transmission Electron Microscopy: Diffraction, Imaging, and Spectrometry" by C. Barry Carter and David B. Williams [8].

2.1 Wave phenomena

Wave equation

Waves are periodic phenomena in both space $\boldsymbol{r}$ and time t. They obey the so-called wave equation:

$$\frac{1}{v^2}\frac{\partial^2\psi(\boldsymbol{r},t)}{\partial t^2} = \nabla^2\psi(\boldsymbol{r},t) \tag{2.1}$$

This equation tells us that the spatial structure $\nabla^2\ \psi$ changes over time $\frac{\partial^2}{\partial t^2}$ while travelling at a certain velocity v.

One solution to Eq. 2.1 is

$$\psi(\boldsymbol{r},t) = a(\boldsymbol{r})\exp\left(i\delta(\boldsymbol{r},t)\right) = a(\boldsymbol{r})\exp\left(i(\boldsymbol{kr}-\omega t+\phi(\boldsymbol{r})\right) \tag{2.2}$$

It describes a wave with an amplitude $a(\boldsymbol{r})$ and a phase $\delta(\boldsymbol{r},t)$. The phase describes the completed fraction of the periodic cycle of a point. The periodicity depends on a wave vector $|\boldsymbol{k}| = \frac{2\pi}{\lambda}$, an angular frequency $\omega = \frac{2\pi}{\nu}$ and a phase shift $\phi(\boldsymbol{r})$. It is possible to create composite types of wave shapes by adding wave functions

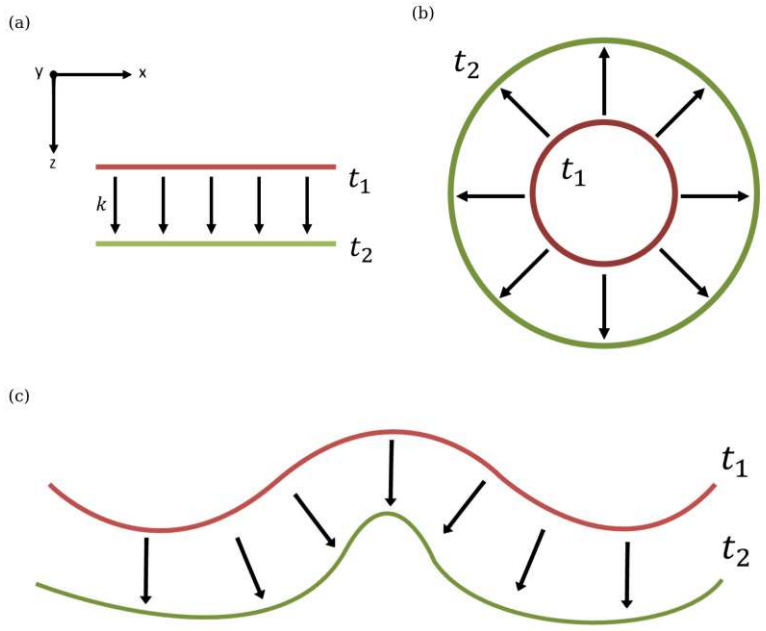

Figure 2.1: A selection of different type of wave fronts starting at time t_1 and propagating in the direction given by the wave vector k. The coloured lines represent the surface of equal phase $\delta(\boldsymbol{r}_i, t_i)$. At a different time t_2, the wave front is still continuous if it was not interrupted by an object. (a) Plane wave (b) Spherical wave (c) Modulated wave

such as Eq. 2.3, which are a solution to Eq. 2.1. What we are interested in is the propagation of the wave front, which is defined as a surface that connects all points of equal phase $\delta(\boldsymbol{r}_i, t_i)$ at a fixed time t_i. Some examples can be seen in Fig. 2.1.

$$\psi(\boldsymbol{r}, t) = \sum_i \psi_i(\boldsymbol{r}, t) = \psi_1(\boldsymbol{r}, t) + \psi_2(\boldsymbol{r}, t) + ... \tag{2.3}$$

Interference

A profound property of waves is their ability to interfere with each other, constructively or destructively, as shown in Fig. 2.2. This is a consequence of Eq. 2.3 as a solution to Eq. 2.1. In experiments, we measure the intensity distribution (for example $|\psi|^2 = |\psi_1 + \psi_2|^2$):

$$I = \psi^*\psi = (\psi_1^* + \psi_2^*)(\psi_1 + \psi_2) = |\psi_1|^2 + |\psi_2|^2 + \psi_1^*\psi_2 + \psi_1\psi_2^* \tag{2.4}$$

The mixed terms $\psi_1^*\psi_2$ and $\psi_1\psi_2^*$ shape the interference pattern. This type of contrast is referred to as "phase contrast" because the measured intensity depends

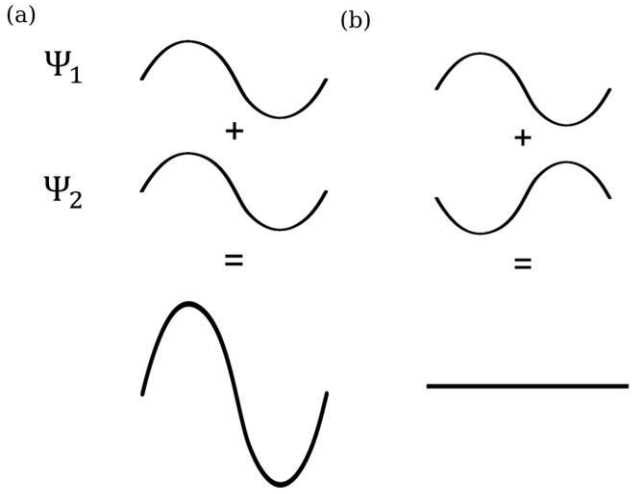

Figure 2.2: (a) Constructive and (b) destructive interference.

on the relative phase difference between the overlapping waves. If the relative phase remains constant, the waves are said to be *coherent* with each other, while random phase fluctuations result in *incoherent* behaviour.

A classic experiment to visualise coherence in interference phenomena is the double-slit experiment performed e.g. by Thomas Young [9]. In theory, a plane wave front passing through a single slit is diffracted to a hemispherical shape. Two slits, separated by a distance g, diffract the plane wave into two hemispherical waves. The overlap produces constructive and destructive interference behind the double-slit, as shown in Fig. 2.3. The relation between the path difference Δx and the fringe spacing s on a screen at a distance d is given by ($d >> g \rightarrow \tan\theta' \approx \sin\theta$):

$$\frac{\Delta x}{g} = \frac{s}{d} \tag{2.5}$$

Electron Matter Waves

Electrons are massive elementary particles with a negative charge. Experiments in the 19th century by William Crookes showed that a beam of accelerated electrons can move a paddle wheel inside a vacuum chamber [10]. Based on this observation, one might conclude that energetic electrons behave as particles. However, the double-slit experiment reveals their wavelike nature. In 1927, C. Davisson and L.H. Germer placed a collimated electron beam onto a single nickel crystal and recorded an angular intensity distribution similar to wave diffraction patterns in

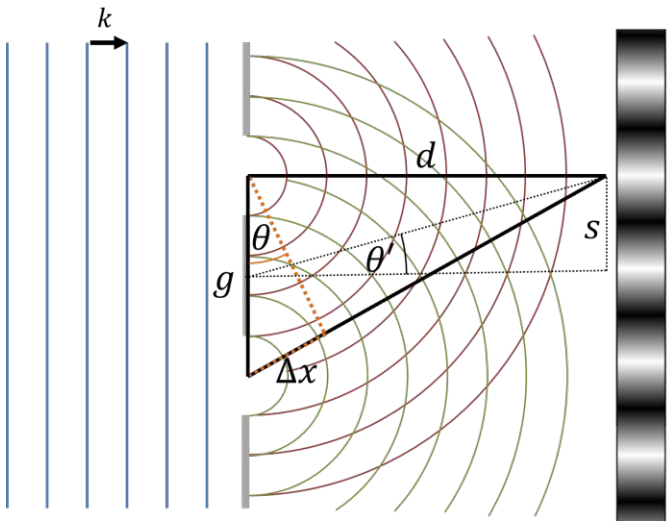

Figure 2.3: Double slit experiment. The relation between the spacing s and the path difference Δx is given by $\frac{\Delta x}{g} = \frac{s}{d}$.

X-ray crystallography [11]. How can we explain the wave behaviour of massive particles? A solution was already found a little bit earlier with the introduction of matter-waves.

The idea of matter-waves originated in 1901 when Planck associated a photon's energy with its frequency ν and the Planck constant h given in units of action [12]:

$$E = h\nu \tag{2.6}$$

This relation led L. de Broglie in 1923 to the idea of assigning a wavelength to particles with rest mass m_0 travelling at a speed $\beta = \frac{v}{c}$, and oscillating at a frequency ν [13]:

$$\nu = \frac{m_0 c^2}{h\sqrt{1-\beta^2}} \tag{2.7}$$

This idea was revolutionary and allowed us to see the Bohr model in a different light. There were some questions left: What does a matter wave look like and does it obey a wave equation? The answer was postulated by Schrödinger [14]:

$$i\hbar\frac{\partial\Psi(\boldsymbol{r},t)}{\partial t} = -\frac{\hbar^2}{2m}\nabla^2\Psi(\boldsymbol{r},t) + V(\boldsymbol{r},t)\Psi(\boldsymbol{r},t) \tag{2.8}$$

This equation describes how the wave function $\Psi(\boldsymbol{r},t)$ evolves over time under the influence of a potential $V(\boldsymbol{r},t)$. Importantly, many principles from classical wave theory remain applicable to matter waves. For example, matter waves can exhibit superposition (Eq.2.3) and interference (Eq.2.4), just like classical waves.

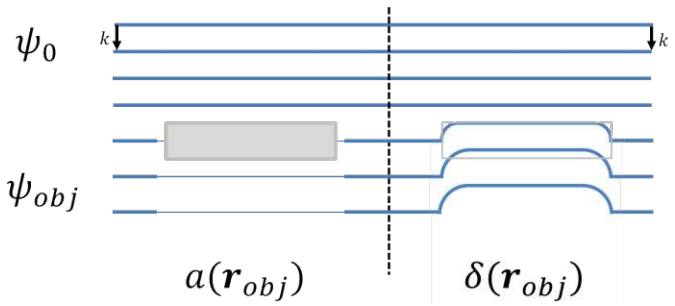

Figure 2.4: Diffraction of a wave by an object. The amplitude $a(\boldsymbol{r}_{\mathrm{obj}})$ of the wave is absorbed by the grey object while the phase $\delta(\boldsymbol{r}_{\mathrm{obj}})$ is shifted. The resulting object wave $\Psi_{\mathrm{obj}}(\boldsymbol{r}_{\mathrm{obj}})$ is the wave that creates the diffraction pattern and the first intermediate image.

These analogies highlight the deep connection between quantum mechanics and wave phenomena.

Eq. 2.7 can be rewritten to calculate a wavelength λ_{dB} for a particle with momentum p:

$$\lambda_{\mathrm{dB}} = \frac{h}{p} = \frac{h}{m_0 \gamma v} \tag{2.9}$$

Inserting numbers for an electron accelerated with 200 kV, $v \approx 0.7c$ ($\gamma = (\sqrt{1-\beta^2})^{-1} = 1.4$) with rest mass energy $m_0 \approx 511\,\mathrm{keV}$, we get $\lambda_{\mathrm{dB}} \approx 2.5\,\mathrm{pm} = 2.5 \cdot 10^{-12}\,\mathrm{m}$, which is about five orders of magnitude smaller than the optical wavelength range ($\approx 10^{-7}$ m) and 20 times smaller than the Bohr radius $a_0 = \frac{\hbar}{m_e \alpha c} = 5.29 \cdot 10^{-11}\,\mathrm{m}$. The FEI Tecnai G20 TEM can achieve a point resolution of $240\,\mathrm{pm} = 2.4 \cdot 10^{-10}$ m in TEM and $150\,\mathrm{nm} = 2 \cdot 10^{-10}$ m in STEM [15], primarily limited by the imperfections in the magnetic lenses and technical constraints.

Image formation and Diffraction pattern

The wave propagating through the object is modulated in amplitude and phase when leaving the object, resulting in the object exit wave $\Psi_{\mathrm{obj}}(\boldsymbol{r}_{\mathrm{obj}})$:

$$\Psi_{\mathrm{obj}}(\boldsymbol{r}_{\mathrm{obj}}) = a(\boldsymbol{r}_{\mathrm{obj}}) \exp(i\delta(\boldsymbol{r}_{\mathrm{obj}})) \cdot \Psi_0(\boldsymbol{r}_{\mathrm{obj}}) \tag{2.10}$$

In the case of electrons, Eq. 2.10 is only valid if the object is much thinner than the inelastic mean free path of electrons inside the object. For example, the inelastic mean free path for 200 keV electrons in silicon is about 150 nm [16], which sets the upper limit of the practical thickness to less than 100 nm for pure phase interactions similar to Fig. 2.4.

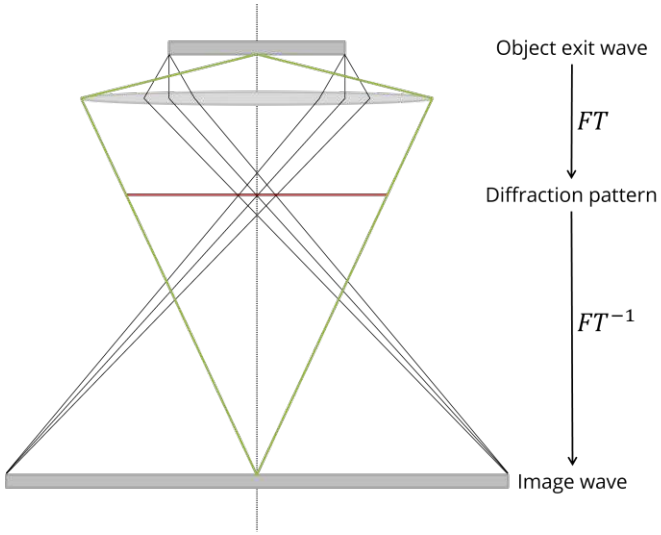

Figure 2.5: Abbe's theory of microscopic imaging. The object exit wave is focused by a lens. In the back focal plane is the location of the diffraction pattern, which corresponds to a Fourier transform in wave mechanics. The first intermediate image is formed below the diffraction pattern. Each additional lens would repeat the schematic.

The objective lens focuses the object exit wave into its back focal plane and forms a diffraction pattern, which corresponds to a Fourier transform in the Fraunhofer far-field approximation and contains the Fourier spectrum of the object exit wave. The image wave is reconstructed in the first intermediate image plane and is the inverse Fourier transform of the diffraction pattern. This concept is known as Abbe's theory and is schematically shown in Fig. 2.5.

2.2 Temporal Correlations in Cathodoluminescence

Cathodoluminescence is light that is emitted in electron-matter interactions. Johann Puluj, one of the pioneers of investigating X-ray radiation with his Pulujlamp, wrote in his book "Strahlende Elektrodenmaterie" (1881) about luminous matter induced by electrons [17]. He and William Crookes suggested a new fourth state of matter, which Puluj called "radiating electron matter" [18]. Today, we understand that various effects can cause radiation (CL), which differ in their underlying process. Some of the most prominent and researched CL excitation processes are listed in a review by Garcia de Abajo [19]. The following sections elaborate on the characteristic electron-photon coincidence signatures of direct emission processes,

referred to as coherent CL, compared to incoherent CL arising from intermediate processes.

2.2.1 Coincidences in Electron-Photon pairs

In experimental physics, a coincidence refers to the detection of signals from two or more detectors that occur within a defined time window. One of the earliest experiments to employ this technique was the Bothe-Geiger experiment [20], which provided evidence about the particle nature of photons by demonstrating that conservation laws are upheld in fundamental scattering processes. Coincidence counting has proven to be a valuable tool for demonstrating the fundamental principles of quantum mechanics. The theory was famously challenged by A. Einstein, B. Podolsky and N. Rosen [21], who questioned whether it provides a complete description of physical reality. It took several decades before John S. Bell formulated a mathematical criterion, known as Bell's inequality, that could be tested experimentally to determine whether nature violates the assumptions of local realism [22]. To test this, J. Clauser et al. proposed an experiment using polarisers, in which coincidence counting could confirm the predictions of quantum mechanics [23]. A subsequent experiment by A. Aspect et al. [24] used correlated photons from a two-photon decay of calcium, producing results that are consistent with quantum mechanics. Finally, the last major experimental loopholes were resolved by B. Hensen et al. [25] and A. Zeilinger et al. [26].

This Master's thesis sets the experimental foundation to perform coincidence experiments with electron-photon pairs in TEM similar to established photonic quantum optics setups, beginning with the search for correlation signals in CL.

Every electron interacting with matter at time t_{e_0} can either coherently produce a photon at $t_{\gamma_0} \approx t_{e_0}$ or excite the specimen that emits a photon after a random lifetime $t_{\gamma_0} \approx t_{\text{life}} \gtrsim t_{e_0}$. In coincidence counting, we record the detection time of electrons $t_e > t_{e_0}$ and photons $t_\gamma > t_{\gamma_0}$, and calculate the time difference $\Delta t = t_\gamma - t_e$. For the purpose of this discussion, we assume that $\Delta t = 0$ corresponds to the expected time difference for coincidences in coherent CL. The number of cross-correlated time differences, $N(\Delta t)$, is visualised in a bidirectional temporal histogram (BTH), examples can be seen in Fig. 3.5f and g. Fig 2.6 illustrates different types of coincidences and their associated temporal correlations.

- $\Delta t < 0$: A photon was emitted before the electron arrived at the sample. There is no causal relation in such electron-photon pairs. This region is dominated by uncorrelated coincidences with an average count of $N_b = \langle N(\Delta t < 0) \rangle$ counts. In the experiment, N_b is considered the background signal.

- $\Delta t \approx 0$: The direct interaction of the electron with the medium induced photon emission. This behaviour is characteristic for direct (coherent) emission processes, where the photon is emitted nearly simultaneously with the electron interaction, within the timing resolution of the setup.

- $\Delta t \approx t_{\text{life}} > 0$: Indirect emission processes are typically characterised by their excitation lifetime. Coincidences in this region resemble a lifetime decay spectrum.

However, Δt strongly depends on the details of how electron-photon pairs are detected. This uncertainty can be represented as a histogram offset δt in Eq. 2.11. The total temporal uncertainty δt accounts for differences in the detection of the time-of-arrival between electron-photon pairs, including all relevant timing jitter and detection response delays. This uncertainty sets the minimum resolvable width of the coincidence window Δt.

$$\Delta t = t_\gamma - t_e = t_{\gamma_0} - t_{e_0} + \delta t \tag{2.11}$$

It is useful to define a metric for the strength of the correlated signal $N_c(\Delta t)$ on top of the uncorrelated background signal $N_b = \langle N(\Delta t < 0) \rangle$. We introduce the degree of correlation $g^2(\Delta t)$, analogous to the degree of coherence in quantum optics [27], as follows:

$$g^2(\Delta t) = \frac{N(\Delta t)}{N_b} = \frac{N_c(\Delta t) + N_b}{N_b} = 1 + \frac{N_c(\Delta t)}{N_b} \tag{2.12}$$

The degree of correlation is quantified by the value of $g^2(\Delta t) > 1$, which indicates the presence of temporally correlated signal. To isolate the number of real coincidences $N_c(\Delta t)$, we subtract the background signal N_b from the total coincidences $N(\Delta t)$. This approach is valid because background coincidences do not exhibit temporal correlation and the background signal contributes equally at $g^2(\Delta t < 0) = 1$ and at $g^2(\Delta t) > 1$. However, this method introduces additional noise, so the results need to be interpreted with caution.

2.2.2 Direct emission

The evanescent electromagnetic fields of a moving electron can directly induce cathodoluminescence when passing through a boundary between two different media (transition radiation) or within a medium in the form of constructive interference of a polarisation field (Cherenkov radiation, diffraction radiation) [19]. In both cases, photon emission occurs on short time scales, typically much shorter than excitation lifetimes $\Delta t < t_{\text{life}} < \text{ns}$. This type of radiation is commonly referred to as coherent CL. It can be distinguished from incoherent CL by analysing

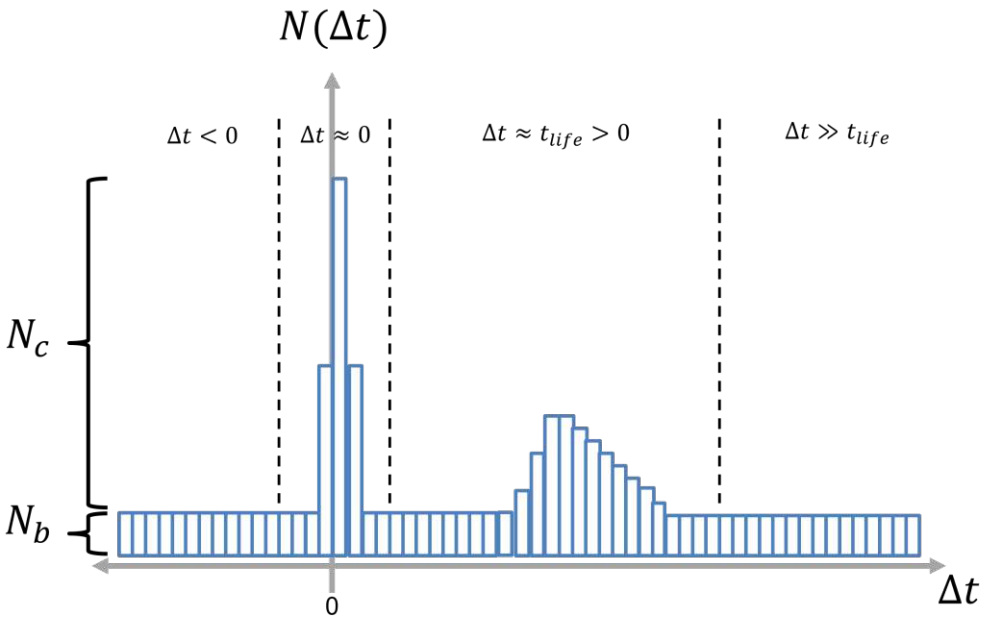

Figure 2.6: Various coincidence windows in a coincidence spectrum. $\Delta t = 0$ corresponds to the ideal detection of the first meaningful coincidence originating from a CL process. Coherent CL is expected in the region $\Delta t \approx 0$, while incoherent CL typically appears at $\Delta t \approx t_{\text{life}}$. However, short-lived excitations may also fall within the coincidence window of coherent CL. These can be distinguished by modifying the experimental setup to analyse energy and momentum relationships in electron-photon pairs, see Fig. 3.5c-e.

the statistical signatures in the second-order correlation function [28] measured in a Hanbury Brown-Twiss interferometer setup (HBT) [29]. The HBT method relies on temporal (anti-)bunching effects of photons, whereas electron-photon coincidences, which do not exhibit (anti-)bunching, can be used to differentiate between coherent and incoherent CL in any emitter. A general mathematical description and an experimental setup using scintillators for electron-photon detection are shown by S. Yanagimoto et al. [30].

The three effects in the following paragraphs should emphasise the similarities of temporal correlation in direct emission processes. They share the property that energy and momentum of the photon are related to an energy loss and a momentum recoil on the initial electron. When the electron-photon time-of-arrival differences are smaller than the smallest resolvable coincidence window, it becomes difficult to identify the dominant process responsible for the observed correlations. However, by using a spatially and temporally resolved electron camera (also applicable with a similar photon camera), the original emission process can be determined by

a characteristic photon emission angle and the corresponding electron deflection angle [31, 32]. This is demonstrated in Ch. 5 and reveals new possibilities in the search for correlated systems.

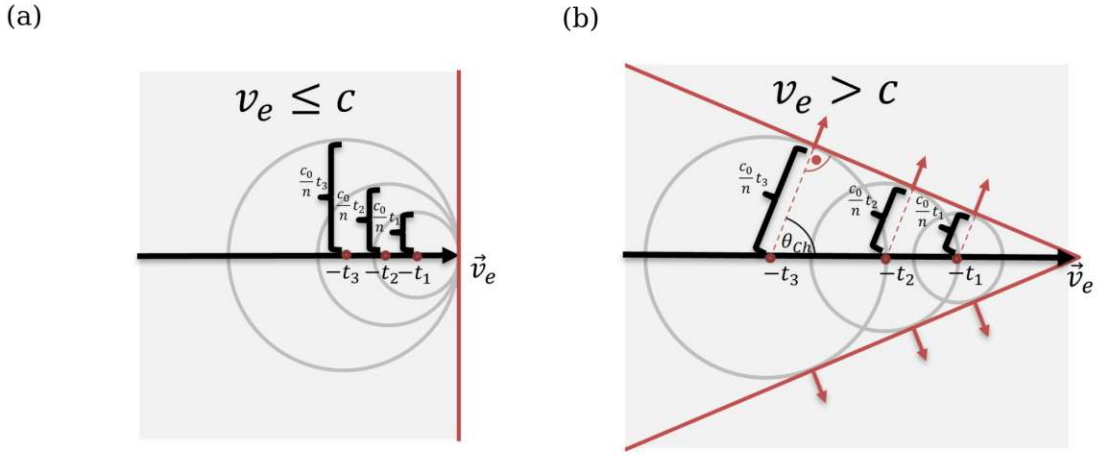

Figure 2.7: Cherenkov radiation. (a) When the electron moves slower than the speed of light, the wavefronts of the polarisation field from the electron bunch together, but they do not constructively interfere. (b) When the electron exceeds the phase velocity of light, the polarisation field forms a wedge-shaped structure with two common tangents, enabling constructive interference and generating Cherenkov radiation at a specific angle, known as the Cherenkov angle.

Cherenkov radiation: When a moving particle with its accompanying electric field enters a medium with a refractive index n, it causes the particles of the medium to polarise according to the orientation of the electric field. The resulting polarisation field can propagate at the reduced speed of light $c = \frac{c_0}{n}$. If the electron moves slower than the reduced speed of light $v_e \leq c$, the wave fronts can bunch but will not overlap (Fig. 2.7a). In the other case $v_e > c$, the wave fronts form a common tangent where they constructively overlap (Fig. 2.7b), inducing the well known Cherenkov radiation [33]. The emission pattern forms a cone shape, similar to the Mach cone in the supersonic boom. The angle at which the Cherenkov photons are emitted is given by the refractive index n and the relativistic speed of the electron $\beta = \frac{v}{c}$:

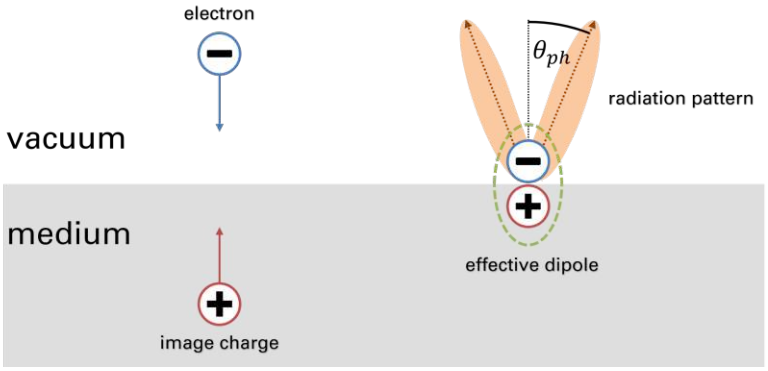

Figure 2.8: Transition radiation. When an electron approaches a surface, it forms an effective dipole with an image charge and radiates a photon when entering the medium.

$$\cos\theta_{\mathrm{ch}} = \frac{1}{\beta n} \tag{2.13}$$

Transition radiation: Transition radiation appears when a charged particle moves through inhomogeneous systems, for example, at the boundary between vacuum and a specimen [34]. Let us assume that an electron approaches a surface, as shown in Fig. 2.8. We can describe the electric field of the situation by introducing an image charge inside the medium with opposite sign and the same distance to the surface as the electron. Before the electron and the image charge merge at the boundary, they form an effective dipole that changes in time as the electron approaches the boundary and vanishes when the electron enters the medium. A photon is emitted in a characteristic dipole pattern. Unlike Cherenkov radiation, transition radiation has no minimum velocity to appear.

Diffraction radiation: Describes radiation that occurs when a charged particle travels near a dielectric or metallic structured surface, but does not physically hit it. The charges in the structure are polarised according to the moving electric fields, similar to Cherenkov radiation. After the electron passes, the polarisation field relaxes, and a photon is emitted. An example of diffraction radiation is given by the Smith-Purcell effect [35], where an electron passes a metal grating and emits photons.

2.2.3 Indirect emission

Indirect emission includes the excitation of an electronic transition in the medium (e.g. atomic transitions, defect transitions, ...) either directly by the electron or by a short-lived mediator particle (e.g. plasmons). After a transition lifetime t_{life}, the excited state relaxes to the ground state by emitting a photon. Due to the intermediate step between electron interaction and photon emission, this type of radiation is inherently incoherent. Furthermore, an electron can trigger a cascade of mediator particles or processes, increasing the chance of a single electron exciting multiple transitions with random lifetimes, emitting photons in various direction. Some examples of typical signatures of incoherent CL are shown by M. Solà-Garcia et al. [36] and I. Vasudevan et al. [37].

There are many other electron-matter interactions that induce indirect emission of CL. For the purpose of illustrating a possible indirect excitation mechanism of a silicon vacancy centre in a micro-diamond, investigated in Ch. 6, we assume that the following process can occur: A mediator particle (plasmon) excites the electronic transition of the vacancy centre (atomic shell transition).

Plasmons: Plasmons are quantised oscillations in the electron density of solid matter. They can occur on the surface (surface plasmon) or inside the medium (bulk plasmon). As plasmons relax to their initial state within a short lifetime, they can excite other electronic transitions or emit a photon if they are surface plasmons. The CL created by the coherent coupling of electrons to surface plasmons shows properties of coherent CL [38].

Atomic shell transition: A free electron can kick a bound electron out of its shell or excite an electron to a higher energy state, leaving a hole. After a certain lifetime, an electron from a higher energetic state occupies the hole and emits the energy difference as an characteristic X-ray photon, shown in Fig. 2.9.

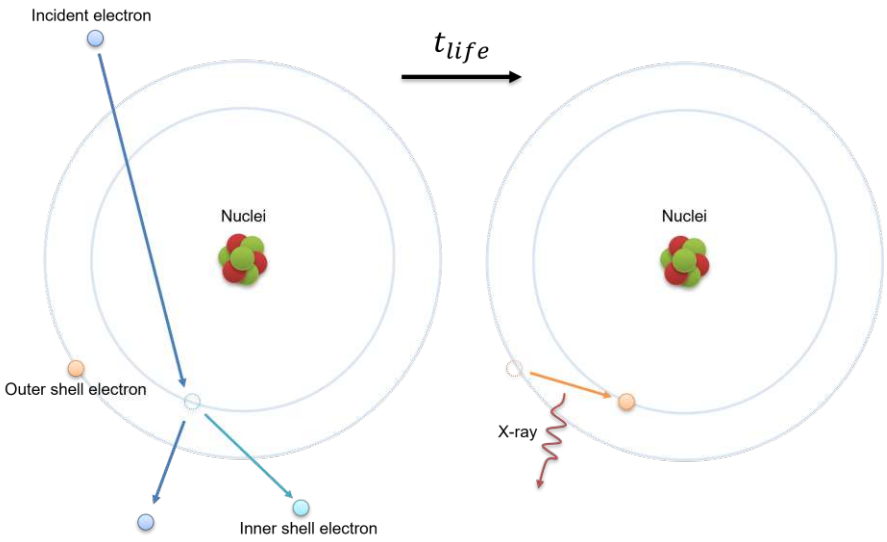

Figure 2.9: X-ray emission from an inner shell excitation. The incident electron kicks out an inner shell electron and leaves a hole. After a characteristic lifetime, an outer shell electron occupies the hole and emits the energy difference as an X-ray photon.

3 Electron Microscopes

During my Master thesis I have been working on TEM, a Transmission Electron Microscope. It is a fascinating device for studying fundamental single-particle processes. Although we note the electron as a particle, it inherits wave-like properties. We can imagine it as looking through an optical microscope. Instead of light at a wavelength of $\approx$ 500 nm, we use fast electrons exhibiting wavelengths on the pm scale, the eyes are replaced with cameras, and the specimen is inserted into a vacuum column. With such microscopes, we can see structures at the atomic scale and interact with them using a focused beam of electrons.

This chapter aims to summarise the operation of a TEM, more precisely the FEI Tecnai G20 located at the University Service centre for Transmission Electron Microscopy (USTEM), shown in Fig. 3.1, and what settings are needed to perform correlation measurements with electron-photon pairs. The sections are based on various chapters from the book "Transmission Electron Microscopy: Diffraction, Imaging, and Spectrometry" by C. Barry Carter and David B. Williams [8].

3.1 Microscope Components

Electron Gun

The part of a TEM that produces the electron beam is an electron gun. The principle is simple: extract an electron from an electron source e.g. a metal and accelerate it with high electric fields. This can be achieved in various ways:

- thermally (heating LaB_6 / tungsten filaments)
- photoelectric effect via pulsed lasers (used in ultrafast TEM)
- high electric field strength (Schottky emitters / tungsten tips / field emission gun)

The FEI Tecnai G20 TEM incorporates an field emission gun (FEG) and can generate electric fields at voltages of up to 200 kV. The electrons are tunnelling from inside the FEG tip into the vacuum and accelerate towards the anode and the accelerator coils. The tungsten tip is also enclosed in an ultra-high vacuum ($< 10^{-9}$ mbar) and kept at a temperature of 1800 K to reduce gas layer formation and

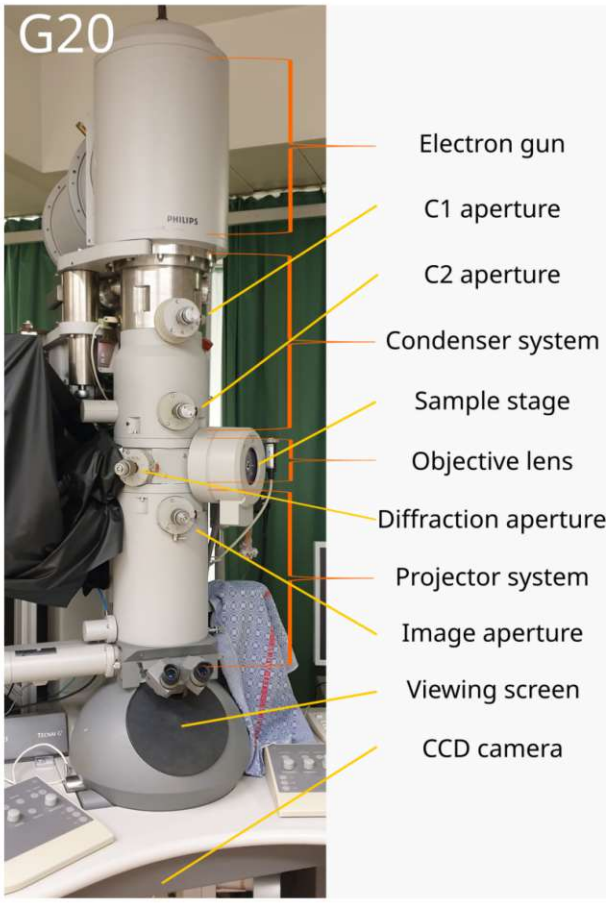

Figure 3.1: FEI Tecnai G20 TEM at USTEM, Freihaus.

maintain the emission characteristics. The resulting electron beam points towards the beginning of the optical system. A vacuum column connects the electron gun to the viewing screen, a CCD camera, or a spectrometer, forming the optical pathway of the TEM.

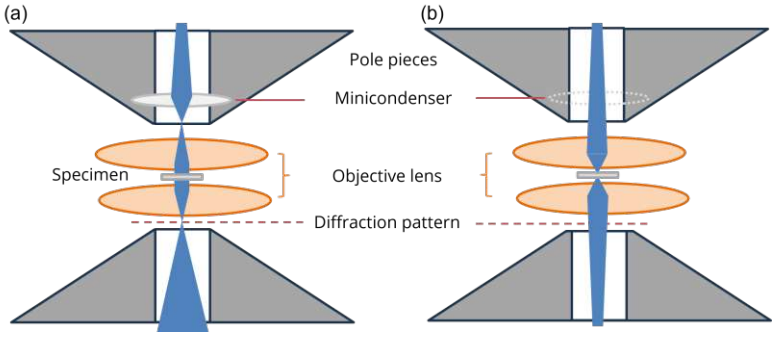

Figure 3.2: Beam operation modes on the FEI Tecnai G20 TEM. (a) A collimated beam is used in TEM mode to illuminate the specimen with a parallel electron beam. (b) A convergent beam is used in STEM mode to scan the specimen. The operation mode can be changed with a minicondenser lens inside the upper pole piece.

Condenser System

The electron beam can be manipulated in the column using magnetic lenses and stigmators, which are essentially coils with an adjustable current. The magnetic fields inside the coil are aligned with the direction of the electron's propagation. The central axis of the magnetic lens, where an electron is not deflected, is called the *optical axis*. Electrons that enter the lens at an angle to the optical axis experience a force that causes them to spiral inside the coil. After passing through the lens, the angle of the electron is reversed and the electron propagates back towards the optical axis, which defines the focal point of the lens. The focal point can be adjusted by controlling the current through the coil. Due to imperfections in magnetic lenses, small stigmator coils are used to improve point resolution.

Once the alignment is set, we can approximately describe the electron beam as a coherent wave hitting the specimen. We adjust the minicondenser and the objective lens to create a collimated (TEM) or a convergent (STEM) beam, as shown in Fig. 3.2.

Sample stage

The CompuStage is the goniometer on the FEI Tecnai G20 to insert a sample holder into the column. It can move the holder tip in the xyz-direction and tilt it around the holder axis. We use the Gatan Vulcan holder, shown in Fig. 3.3a, for the here presented experiments to extract CL, which is guided over multi-mode fibres onto dedicated fibre ports for the top and bottom mirrors. This allows photons that were emitted between the pole pieces in Fig. 3.3b to be guided out of the column.

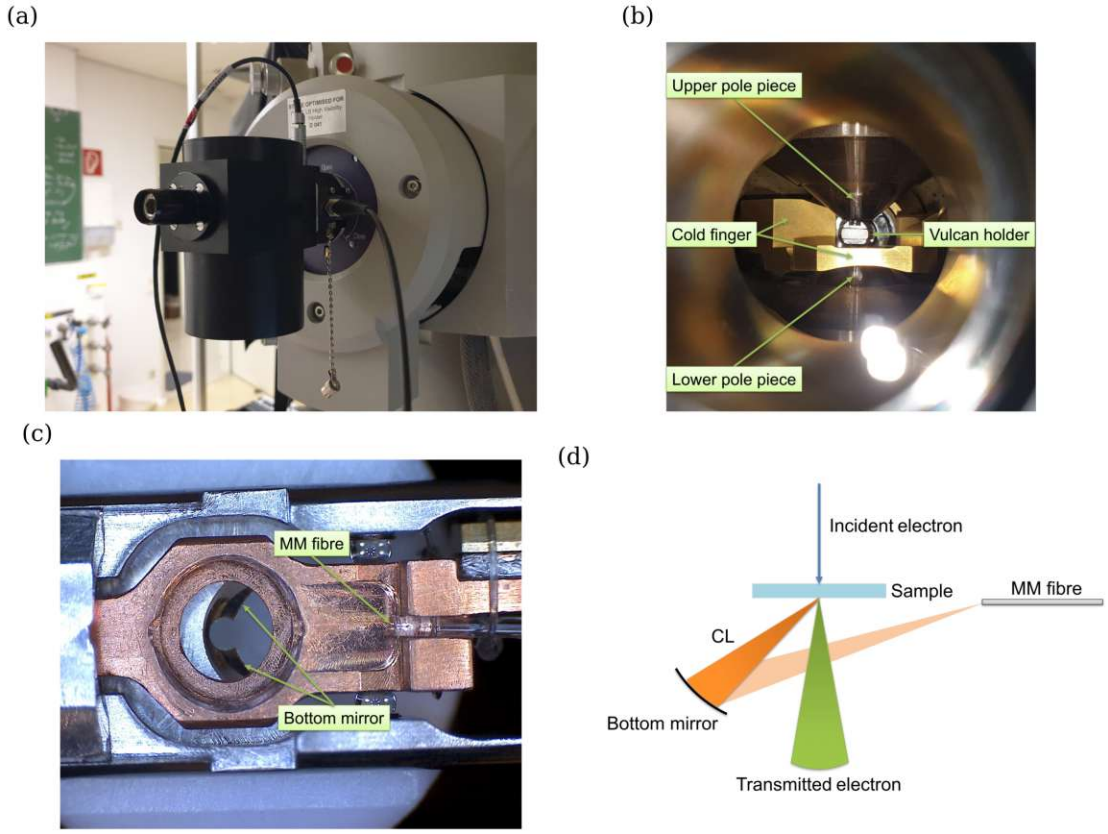

Figure 3.3: Gatan Vulcan holder inserted into the column, which allows to fibre couple CL. (a) On the outside, the multi-mode fibres can be attached to either the CL collecting top or bottom mirror. (b) The holder tip with the mirrors is positioned between the pole pieces, with a gap of 5.4 mm between them. The cold finger surrounds the holder tip and is cooled using liquid nitrogen to reduce contamination. (c) Elliptical mirrors are positioned above and below the sample. The top mirror can be moved to insert a specimen. (d) The two focal points of the elliptical Vulcan mirrors are designed to coincide with the specimen and the facet of a multi-mode fibre, respectively.

Gatan Vulcan

The Gatan Vulcan system is a fibre-based optical CL system. It consists of elliptical mirrors above and below the specimen to collect CL (Fig. 3.3c), directing the light into multi-mode fibres (Fig. 3.3d), which are then guided to an optical spectrometer. Here, we can acquire an optical spectrum using a CCD camera or record photon counts per second with a water-cooled photomultiplier tube (PMT) while scanning the specimen (STEM).

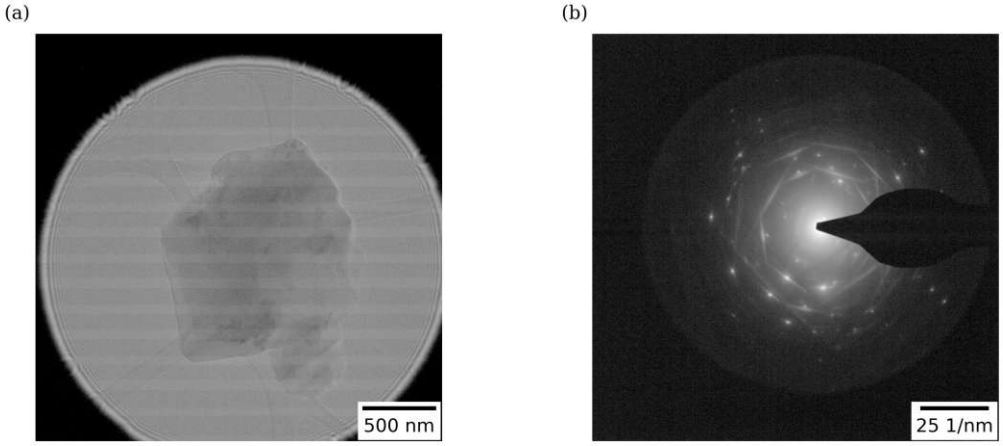

Figure 3.4: (a) The projection of the first intermediate image. It shows a low contrast picture of a micro-diamond which has been investigated in Sec 6.4. (b) With a push of a button, we can change the lens settings of the projection system and see the diffraction pattern.

Projection system

The projection system magnifies the first intermediate image onto the viewing screen or a detector, e.g. a CCD camera (Fig. 3.4a). We can also record the diffraction pattern (Fig. 3.4b) by changing the lens settings in the projector system without influencing the beam above the sample.

Spectrometer

An electron spectrometer incorporates a magnetic prism to disperse the electron beam for analysis of the energy dispersive spectrum of the object exit wave. Electrons that interacted inelastically transfer or gain kinetic energy, causing them to either speed up or slow down. This affects their trajectories in the magnetic prism due to the velocity-dependent Lorentz force. The energy-dispersed electron beam is afterwards captured by a time-resolved Timepix3 (TP3) camera.

The spectrometer offers two different operation modes: energy-filtered TEM (EFTEM) and electron energy loss spectroscopy (EELS). In both EFTEM and EELS, electrons are dispersed based on their energy loss. In EFTEM, this dispersion is used to form energy-filtered images by selecting electrons within a specific energy window, enabling spatially resolved chemical or elemental mapping. In EELS, the dispersed electrons are projected onto a detector to produce a spectrum, providing detailed information about the sample's electronic structure and composition. Examples can be seen in Sec. 6.4 for EFTEM and Sec. 6.3 for EELS.

3.2 Coincidence Electron Microscopy

Experimental Setup

Fig. 3.5 illustrates a general schematic of coincidence electron microscopy. An electron beam from the electron source (blue beam) in the FEI Tecnai G20 TEM propagates through the column and is shaped by magnetic coils and apertures (Fig. 3.5a). The electron hits a specimen in the sample plane of the microscope (Fig. 3.5b) and can induce coherent or incoherent cathodoluminescence from various excitation mechanisms (Fig. 3.5c-e). Each process can be characterised by the time difference $\Delta t = t_\gamma - t_e$ between the electron interaction time t_e and the photon emission time t_γ. The electron can lose kinetic energy due to the specimen interaction (energy conservation, green beam) and continues towards a magnetic prism, which disperses the trajectory of the electron depending on the energy loss. Afterwards, the Time of Arrival (ToA), Time over Threshold (ToT) and position of the electron are recorded by the TP3, which is mounted on a TV port of the Gatan GIF 2001 spectrometer behind an energy-selective slit.

The photons (orange beam) are coupled into multi-mode fibres by an elliptical mirror of the Gatan Vulcan holder and guided outside of the TEM. Optical filters [39] can be placed in a multi-mode filter holder (Fig. 3.7f) before being directed to a single photon counting module (SPCM). The electron and photon time stamps are synchronised using a Time Tagger Ultra (TT), which utilises the 40 MHz clock and a trigger output signal from TP3, see Fig. 3.8. A bidirectional temporal histogram (BTH) visualises the number of detected coincidences within a given coincidence window Δt, revealing signals from temporally correlated electron-photon pairs (Fig. 3.5f and g).

A convenient formula to relate photon wavelengths to an energy is given by:

$$\lambda_\gamma = \frac{hc}{E_\gamma[\mathrm{J}]} = \frac{hc}{E_\gamma[\mathrm{eV}] * 1.602 \cdot 10^{-19}[\mathrm{J\,eV^{-1}}]} \tag{3.1}$$

$$\lambda_\gamma[\mathrm{nm}] \approx \frac{1240[\mathrm{eV\,nm}]}{E_\gamma[\mathrm{eV}]} \tag{3.2}$$

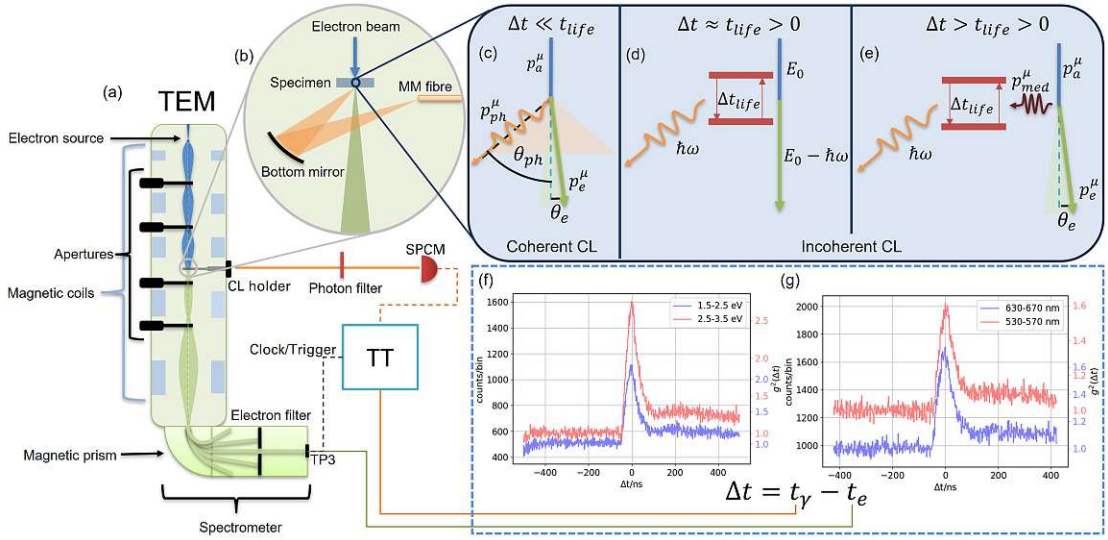

Figure 3.5: Coincidence Microscopy overview. (a) In TEM, the electron beam (blue) is shaped inside a vacuum column with apertures and magnetic coils. Electrons interact with a specimen in the object plane of the microscope and can induce CL. The transmitted electron beam (green) is dispersed in a magnetic prism (energy filter), which allows for energy selective electron detection on TP3. A CL holder guides photons towards an optional photon filter and a single photon counting module. The electron (t_e) and photon (t_γ) time tags are synchronised with the clock and trigger output signal of TP3 via a time tagging unit. (b) Inside the CL holder, photons (orange) emitted from the specimen are reflected from the bottom mirror and coupled into multi-mode fibres. (c) Coherent CL is characterised by an energy and momentum relationship in electron-photon pairs that are detected within a small coincidence window. (d,e) In incoherent CL, the electron-photon time difference depends on the intermediate steps of the photon emission. Electron-photon correlations can be analysed in detail by either energy-filtering the electrons (f), the photons (g) or both.

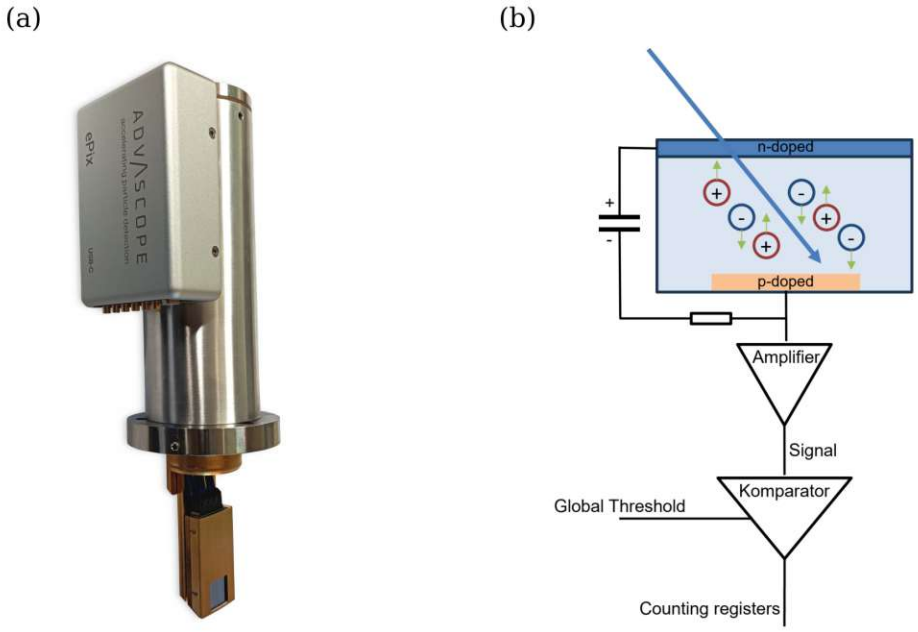

Figure 3.6: (a) Advascope ePix [40]. The TP3 chip is located inside the rectangular window on the bottom side, consisting of 256 x 256 pixel detectors. A schematic of a single pixel detector is shown in (b). When a charged particle (blue arrow) enters the silicon chip, it generates electron-hole pairs. A bias voltage is applied to the n-doped top layer and the 55 x 55 μm^2 sized p-doped layer. The holes diffuse toward the n-doped top layer, and the electrons move to the nearest p-doped layer. The signal is increased by an amplifier, and the output of the comparator is activated if the signal exceeds a programmable global threshold voltage. Counting registers then record the position, Time of Arrival (ToA) and Time over Threshold (ToT) of the excited pixels.

The following electron and photon detection devices have been used for the experiment:

Electron Detection:

The Advascope ePix is a pixel detector from Advascope [40] based on Timepix3 technology [41] developed by the medipix collaboration at CERN [42]. An electron event is detected by 55 x 55 μm^2 pixel detectors in a 256 x 256 pixel array (Fig. 3.6b). The data read-out design allows for the setting of a detection threshold for almost unitary detection efficiency on the nanosecond scale. It has a timestamp precision of 1.5625 ns and can register up to 64 million events per second.

Photon Detection:

The Excelitas SPCM-AQRH-14 (Fig. 3.7a) is a highly efficient single photon counting module with detection efficiencies up to 70 % at 650 nm (Fig. 3.7b). It employs a 180 µm diameter active-area photodiode for detecting photons in the 400-1060 nm wavelength range. The intensity saturation is reached at 37 million counts per second and exhibits a 350 ps jitter at 825 nm. Our device shows a typical dark count rate of 50 counts per second.

The PicoQuant Photon Multiplier Assembly (PMA) Hybrid detector is a Peltier-cooled photocathode with a large active sensor diameter of 5 mm combined with a photomultiplier tube (Fig. 3.7c). Our device is optimised for 300-780 nm photons with a peak detection efficiency of 40% between 450 and 600 nm (Fig. 3.7d) at an average dark count rate of 130 counts per second. The manufacturer's recommended maximum count rate is specified at 10 million counts per second with a typical jitter below 120 ps.

Time Tagger:

The Time Tagger Ultra (TT) by Swabian Instruments [43] (Fig. 3.7e) detects incoming electrical signals and marks the events with time stamps at 42 ps rms jitter. The input channels are freely programmable and can be used for setting different threshold voltages, triggering on rising or falling edges and synchronising multiple time tag streams. A data acquisition script can be coded with Python by using available packages and manuals provided by Advascope [44] and Swabian Instruments [45]. The data is saved in files containing approximately 650k electron events each and the corresponding photon time stamps. Both sets are synchronised using the trigger signal of the TP3, see Fig. 3.8.

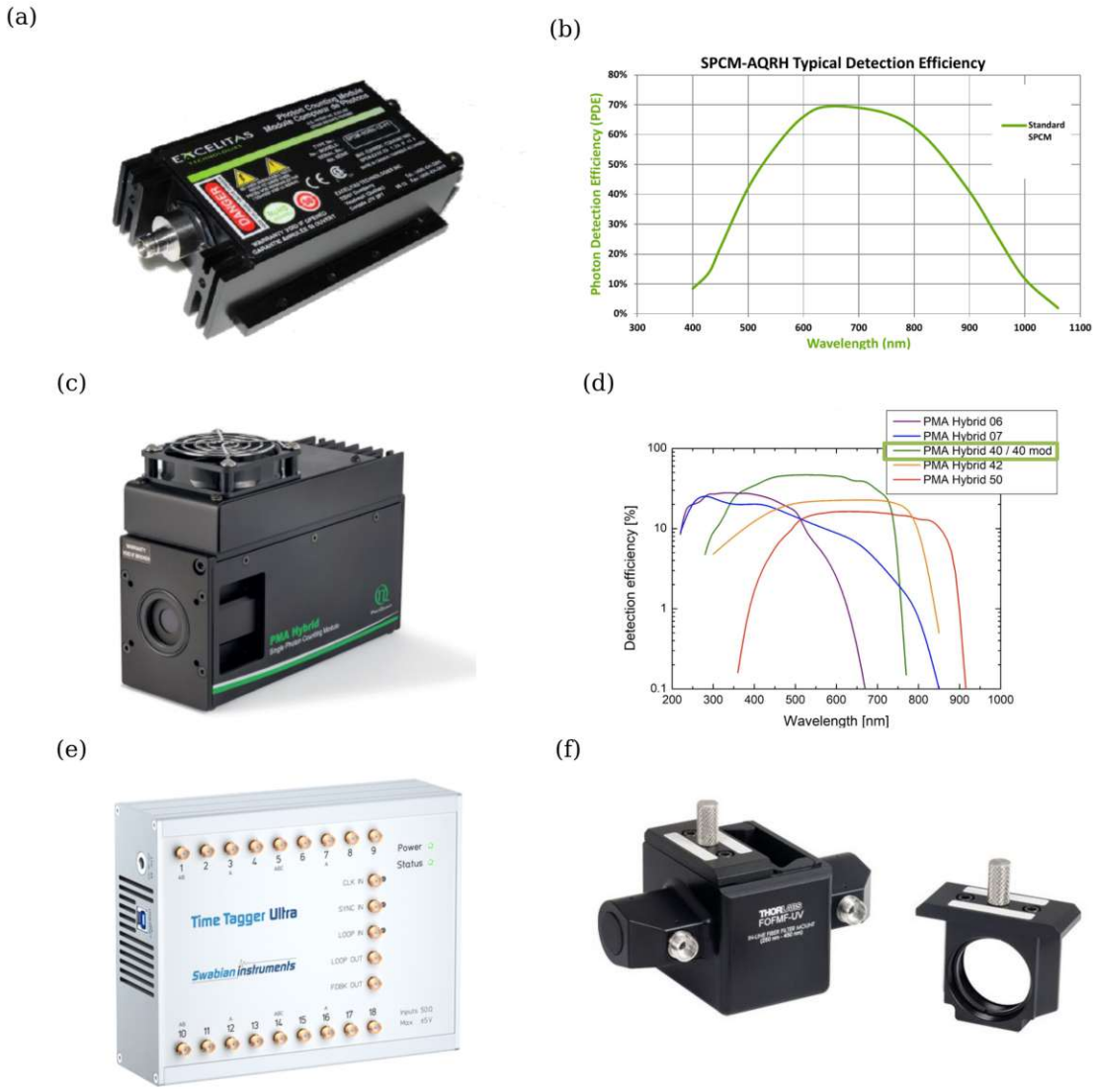

Figure 3.7: (a) Excelitas SPCM-AQRH-14 [46]. (b) Detection efficiency of a typical Excelitas SPCM [46]. (c) Picoquant PMA Hybrid series [47]. (d) Detection efficiency of the Picoquant PMA Hybrid series [47]. The green line represents the model used. (e) Time Tagger Ultra by Swabian Instruments [43]. (f) Optical Filter holder by Thorlabs [48].

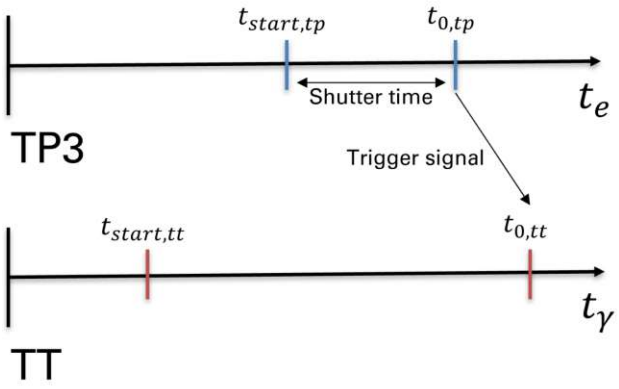

Figure 3.8: Synchronization of the TP3 and TT. When the TT is first initialized in the code, its internal clock starts ($t_{start,tt}$). The clock of the TP3 starts after the clock synchronisation with the TT ($t_{start,tp}$). Once the TP3 starts data acquisition after the shutter time ($t_{0,tp}$), it sends out the trigger signal, which is detected by the TT ($t_{0,tt}$) and both data packages have an absolute time reference.

The last step is the search for coincidences with the following variables:

- `electrons`: time stamps of detected electrons
- `photons`: time stamps of detected photons
- `offset`: $\equiv \delta t$ in Eq. 2.11
- `COIN_WINDOW`: half-width of the coincidence window, defining the temporal range within which events are considered correlated

The coincidences are calculated using the following lines:

```
 # Calculate matrix of all relative time differences
diff_arr = photons - electrons[:,np.newaxis] - offset

# Filter for electron positions inside the coincidence window
xy_arr = (diff_arr > -COIN_WINDOW) & (diff_arr < COIN_WINDOW)
```

Listing 3.1: Coincidence filtering

With these two lines of code, we can simultaneously compute the data for the BTH and extract the impact locations of each coincident electron event. This enables for flexible data processing and storage solutions.

4 Calibration of Timepix3

Timepix3 (TP3) is a silicon-based 256 x 256 pixel array detector with nearly unitary detection efficiency. When a highly energetic particle hits the chip sensor, the read-out electronics register both the time-of-arrival (ToA) and energy deposition (ToT) per pixel. To ensure high timing accuracy and precision across the entire chip area, a calibration routine is required. Our routine includes an energy calibration and a time-walk correction, which will be elaborated in this chapter. The calibration can be performed with X-ray sources [49], a linear accelerator [50] or with a tunable electron beam [51]. The FEI Tecnai G20 TEM, capable of providing high-voltages as low as 6 kV [15], is particularly useful for parameter fitting close to the programmable detection threshold of the TP3. Following calibration, the timing stability of TP3 is assessed using a specialised TEM holder which can create an oscillating electron beam.

4.1 Clustering

After interaction of an electron with the pixel, the TP3 chip collects the charges during a fixed integration time. The time-of-arrival (ToA) is registered if the signal climbs above the programmable threshold and starts the counter for the time-over-threshold (ToT). The complete response schematic is shown in Fig. 4.1a.

We have to consider that an electron might scatter over multiple pixels at once, which results in clustered events such as Cluster 2 in Fig. 4.1b. The sum of the energies inside the cluster should correspond to the initial electron energy. Because each pixel has an individual energy-ToT response curve, a pixel-per-pixel energy-calibration routine is needed to provide comparable pixel energy values. Our calibration will use Cluster 1 for energy calibration and Cluster 2 for time-walk correction. The clusters are sampled by the `DBCAN` algorithm [52].

Fig. 4.2 shows the average raw ToT distribution of all pixels from the calibration data sets ranging from an initial beam energy of 7 to 60 keV in Fig. 4.2a and 80 to 200 keV in Fig. 4.2b. The global detection threshold is set to 6 kV, ensuring a good signal-to-noise ratio when no electron beam is directed onto the TP3. The electron beam is spread across the entire chip surface at a current below 5 pA ($\approx 30 \cdot 10^6 \frac{e^-}{s}$) while data sets are acquired for 10 seconds in each setting. A low beam current prevents data saturation of the TP3, which can handle up to 64 million events

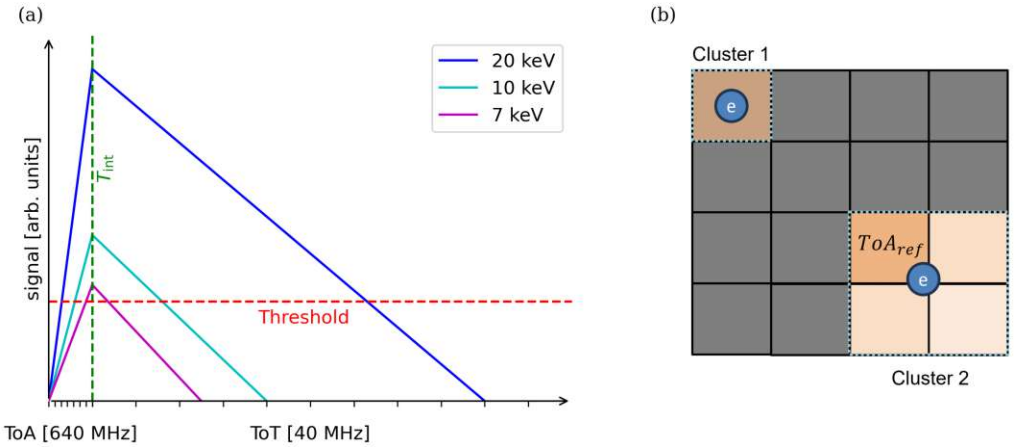

Figure 4.1: Schematic of an event detection. (a) The ToA is defined by the time in which the output voltage of the pixel amplifier exceeds the threshold value. At this moment, a 640 MHz clock (= 1.5625 ns) is activated until the fixed integration time T_{int} is reached. The ToT counts the global clock cycles (40 MHz = 25 ns) where the pixel potential is above the threshold voltage. (b) An electron can either hit a single pixel (Cluster 1) or scatter across multiple pixels (Cluster 2). To correct for time differences between neighbouring pixels in a clustered event, known as time-walk, the pixel with the highest ToT value is used as the reference time stamp ToA_{ref} for the time-walk calibration.

per second, and increases the probability of spatially and temporally separated clustered events for subsequent calibration steps.

In Fig. 4.2a and b, the peaks broaden with increasing acceleration voltage because higher-energy electrons deposit their energy over a larger volume. An interesting observation at acceleration voltages above 100 keV, shown in Fig.4.2b, is the flattening of the peaks above 200 ToT cycles at 100, 120, and 140 keV, while a new peak at 100 ToT cycles emerges at 160, 180, and 200 keV.

In summary, higher acceleration voltages result in a greater occurrence of clustered events, as seen in Fig. 4.2c, which in turn limits the maximum useable electron current.

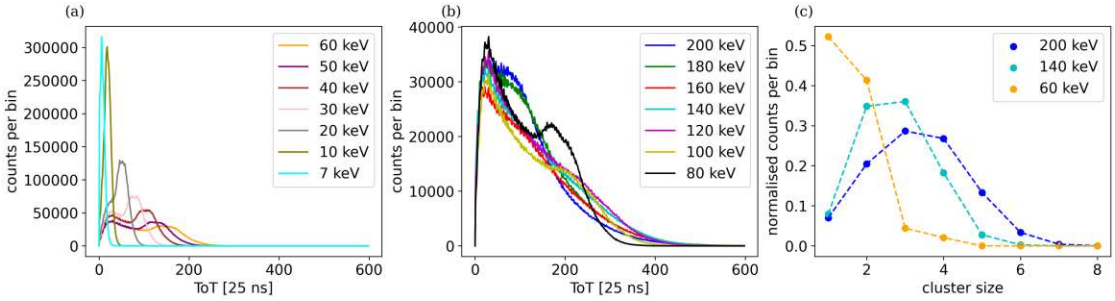

Figure 4.2: Raw data for energy calibration. The data has been acquired with one aperture and electron gun setting (Gun lens 8, Spot size 8) for 10 seconds at each acceleration voltage setting. (a) From 7 to 60 keV, each distribution shows a peak that decreases in height towards higher ToT values. (b) From 80 to 200 keV, the distributions flatten out and broaden. (c) When we analyse the data in terms of clustered events, meaning multiple pixels recorded the same electron, it shows an increased probability of clustered events at higher electron energies. The sum of energies inside clustered events should correspond to the initial electron beam energy after calibration.

4.2 Energy Calibration

Fig. 4.3a and b illustrate the parameter fitting of the energy-ToT response curve per pixel. Similarly to Fig. 4.2a and b, we evaluate the ToT distribution for each pixel of the matrix at a position (x, y) and save the ToT value with the highest counts. Some of the typical ToT values from different pixels are plotted as dots in Fig. 4.3a. The ToT values increase linearly with the electron high tension above 10 keV while they accumulate below 10 keV toward the global threshold of 6 keV. This indicates that the fitting curve should account for the non-linear behaviour below 10 keV, transitioning to a linear curve above 10 kV. A function that satisfies this requirements is given by [50]:

$$ToT(E, x, y) = a_{\text{tot}}(x, y) \cdot E + b_{\text{tot}}(x, y) - \frac{c_{\text{tot}}(x, y)}{E - d_{\text{tot}}(x, y)} \tag{4.1}$$

A single pixel at position *(x,y)* exhibits a ToT time $ToT(E, x, y)$ if it is hit by an electron with kinetic energy E assuming it is absorbing all the electron's energy. The fitting parameter $a_{\text{tot}}(x, y)$ describes the sensitivity of the pixel, $b_{\text{tot}}(x, y)$ is an offset correction, $c_{\text{tot}}(x, y)$ and $d_{\text{tot}}(x, y)$ model the non-linear behaviour close to the threshold.

We use the `curve_fit` function of the `scipy.optimize` package [53] to receive the fitting parameters $a_{\text{tot}}(x, y)$, $b_{\text{tot}}(x, y)$, $c_{\text{tot}}(x, y)$, $d_{\text{tot}}(x, y)$ for Eq. 4.1. These parameters form the pixel energy response curve in Fig. 4.3a. Fig. 4.3b are the

a_{tot} values corresponding to the sensitivity of each pixel of TP3. There are three distinct regions: A spot in the middle, a circle around the centre spot, and the corners outside the circle. The reason for this lies in the previous usage of the camera. The central spot is caused by experiments that require focused beams in the centre of the chip surface (see Sec. 5.2), which induces material degradation. The circle around the central spot is the shape of the spectrometer entrance aperture, which was the maximally illuminated area before adjusting the magnification coils to cover the whole chip.

To convert the ToT value of a pixel at position (x, y) to an energy E in keV, we use the inverse function of Eq. 4.1 ($a_{\mathrm{tot}} = a_{\mathrm{tot}}(x, y)$, $b_{\mathrm{tot}} = b_{\mathrm{tot}}(x, y)$, etc.):

$$E(ToT, x, y) = \frac{ToT + a_{\mathrm{tot}} d_{\mathrm{tot}} - b_{\mathrm{tot}} + \sqrt{(b_{\mathrm{tot}} + a_{\mathrm{tot}} d_{\mathrm{tot}} - ToT)^2 + 4 a_{\mathrm{tot}} c_{\mathrm{tot}}}}{2\, a_{\mathrm{tot}}} \tag{4.2}$$

Inserting the parameters results in the energy-ToT response curves shown in Fig. 4.3a as the solid lines.

Fig. 4.4a and b shows the average energy absorbed by a single pixel at different high tension settings after calibration. Each plot is normalised such that the maximum value equals one, allowing us to compare whether the most common energy value corresponds to the initial electron energy. Up to 60 keV (Fig. 4.4a), the peak of each data set agrees with the initial electron beam energy. Above 80 keV (Fig. 4.4b), most pixels do not absorb the full energy of the initial electron. This means that identifying and evaluating clustered events becomes necessary at high acceleration voltages.

Fig. 4.4c shows the final result of the energy calibration, including the total energy in clustered events. The magnitude of each curve now aligns to the expected energy values of each data set. By examining the amplitudes of 180 and 200 keV, we estimate that the energy calibration achieves a resolution of 20 keV at 200 keV (EDX $\Delta E \approx 150$ eV, EELS $\Delta E < 1$ eV). The resolution could be further improved by implementing a fitting routine on the raw data to determine the statistical mean of the ToT values.

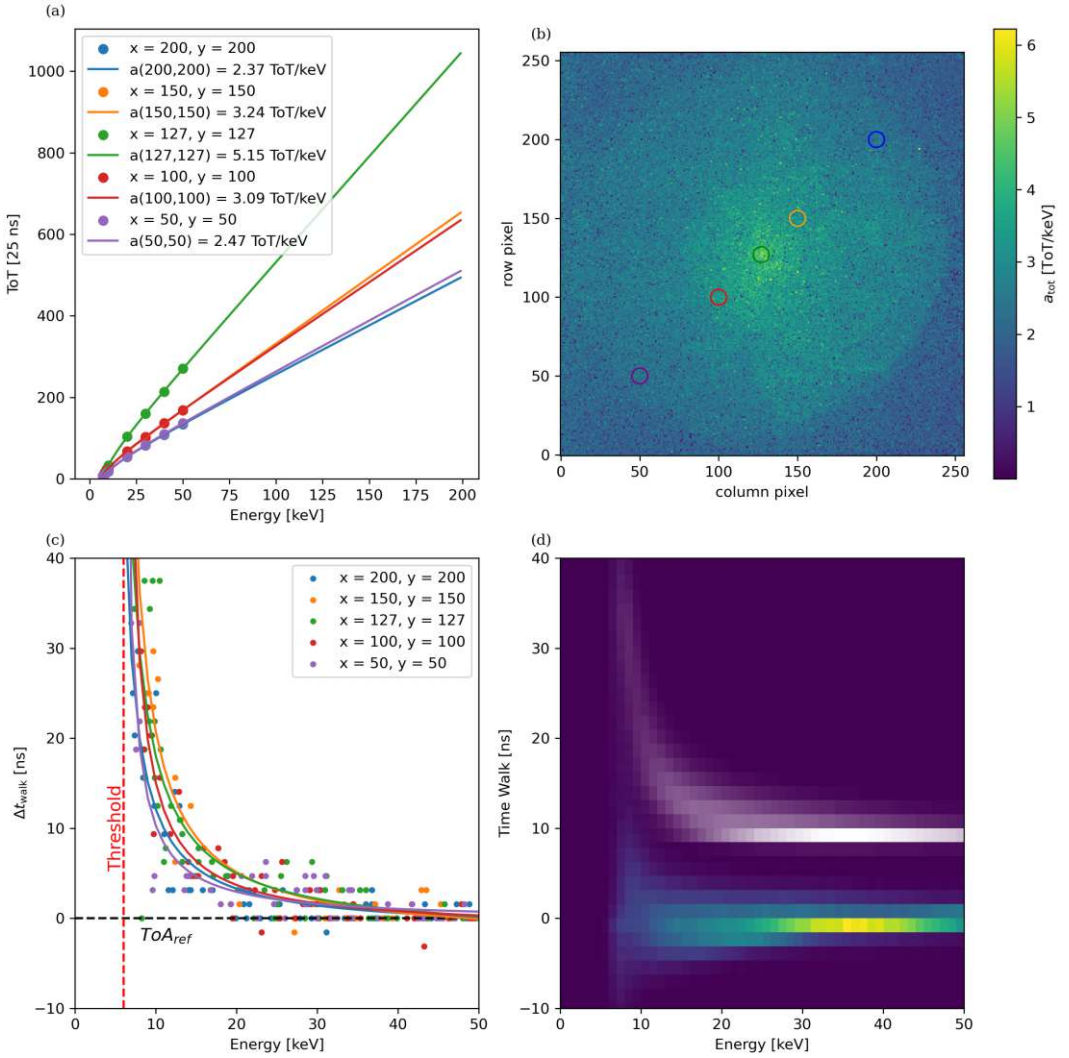

Figure 4.3: Energy and time-walk calibration. (a) Energy calibration for different pixels at position *(x,y)* in the pixel matrix of TP3. The x-axis of the plot marks the incident beam energy setting. Each dot is the most common ToT value per pixel *(x,y)* with respect to the initial beam energy. The fitting curves (solid lines) extrapolate the ToT values up to 200 keV. In reality, a single pixel only absorbs deposited energies sufficiently up to 80 keV, see Fig. 4.4b. (b) The a_{tot} parameter matrix contains the pixel-per-pixel parameters for the energy sensitivity. The effects of beam irradiation caused by previous usage is visible. (c) Time-walk curve fitting for single pixels *(x,y)*. The x-axis corresponds to the absorbed energy per pixel. (d) Time-walk effect averaged over all pixels with (yellow-green) and without (white) correction.

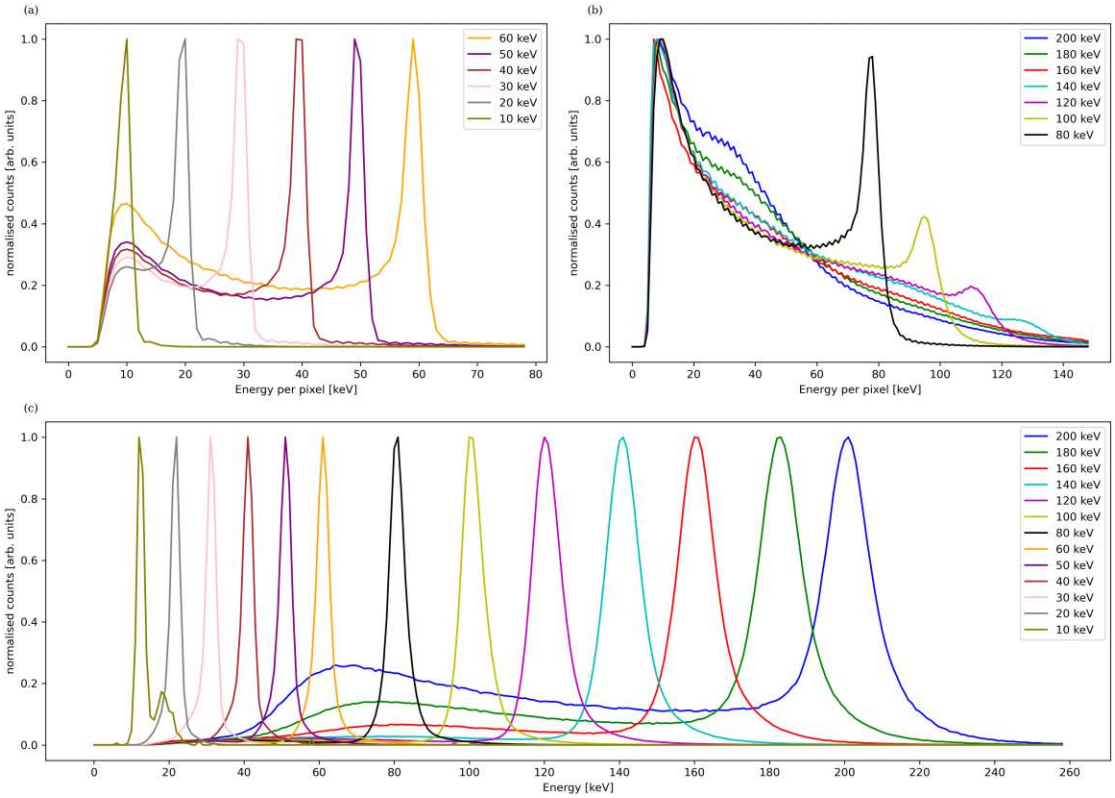

Figure 4.4: Energy calibration results. (a) The coloured lines represent the initial electron beam energy setting. The plot illustrates the average energy absorbed by a single pixel detector for initial beam energy between 10 - 60 keV, after calibration. The peak values show good agreement with the initial electron beam energy. (b) Average energy absorbed by a single pixel for 80 - 200 keV energy after calibration. Towards high initial beam energies, there is a decline in the average amount of energy that a single pixel is exposed to. This is an indication that higher energetic electrons are more likely to scatter over multiple pixels. (c) The plot shows the final energy response of the calibrated TP3 chip for initial electron energy ranging from 10 - 200 keV, including the total energy absorbed in clustered events.

4.3 Time Walk Correction

After the energy calibration, we obtain knowledge about the energy resolution of TP3, seen in Fig. 4.4c. This will have an influence on the timing precision of the ToA which depends on the first crossing of the amplifier signal above the global threshold in Fig. 4.1a. The time delay between the electron impact and the initial event detection, known as the time-walk effect (TW), is a crucial correction for

assigning a representative ToA value to clustered events and compensating single-pixel clock offsets.

Fig. 4.3c shows the time-walk effect for individual pixels at a position (x, y) as dots and the pixel-per-pixel correction curves in solid lines. The time-walk in a Cluster 2 is determined by the time difference between the reference pixel with the highest ToT value (ToA_{ref}) and the surrounding pixels (ToA_i). The clusters are sampled by the `DBSCAN` algorithm with a minimum size of two events per cluster. In Fig. 4.3c, the scatter plot illustrates the distribution of time differences Δt_{walk} within clustered events $\Delta t_{\text{walk},i} = ToA_i - ToA_{\text{ref}}$ depending on the absorbed energy of each individual pixel. The ToA differences within clustered events grow rapidly as the absorbed energy approaches 6 keV energy. This behaviour is due to the global detection threshold being set at 6 keV. The time-walk effect becomes more pronounced just above this threshold, leading to potential inaccuracies in the ToA data of up to 45 ns, particularly in pixels that absorb only a small amount of energy, if left uncorrected. A fitting function that compensates the TW is given by [50]:

$$TW(E, x, y) = b_{\text{toa}}(x, y) + \frac{c_{\text{toa}}(x, y)}{E - d_{\text{toa}}(x, y)} \tag{4.3}$$

This function gives us the amount of offset $TW(E, x, y)$ we have to subtract from the ToA of a pixel at *(x,y)* caused by the time-walk effect depending on the absorbed amount of energy *E*. The parameters $c_{\text{toa}}(x, y)$ and $d_{\text{toa}}(x, y)$ control the steepness of the time-walk effect close to the threshold, $b_{\text{toa}}(x, y)$ accounts for the primary base offset. The pixel-per-pixel time-walk data is given to the `curve_fit` function to get the parameters for the time-walk correction function Eq. 4.3 per pixel.

Fig. 4.3d shows the result of the time-walk correction. The white line is the uncorrected time-walk effect across the entire chip, shifted to +10 ns for clarity. The time-walk correction reduces the ToA uncertainty to about ± 5 ns at 10 keV electron energy, seen as the yellow-green distribution,. This highlights the importance of the time-walk correction for high energies where clustered events are unavoidable and need to be calibrated to guarantee high timing precision.

4.4 Temporal Calibration

Finally, we aim to verify the temporal calibration for coincidence measurements. One approach is to collect temporal electron-photon data from a sample and then analyse the temporal cross-correlation histogram, shown in Y. Auad et al. [51]. We utilise a newly developed TEM holder with a micro-coil around the path of the electron beam, which was designed to detect electron spin resonance (ESR)

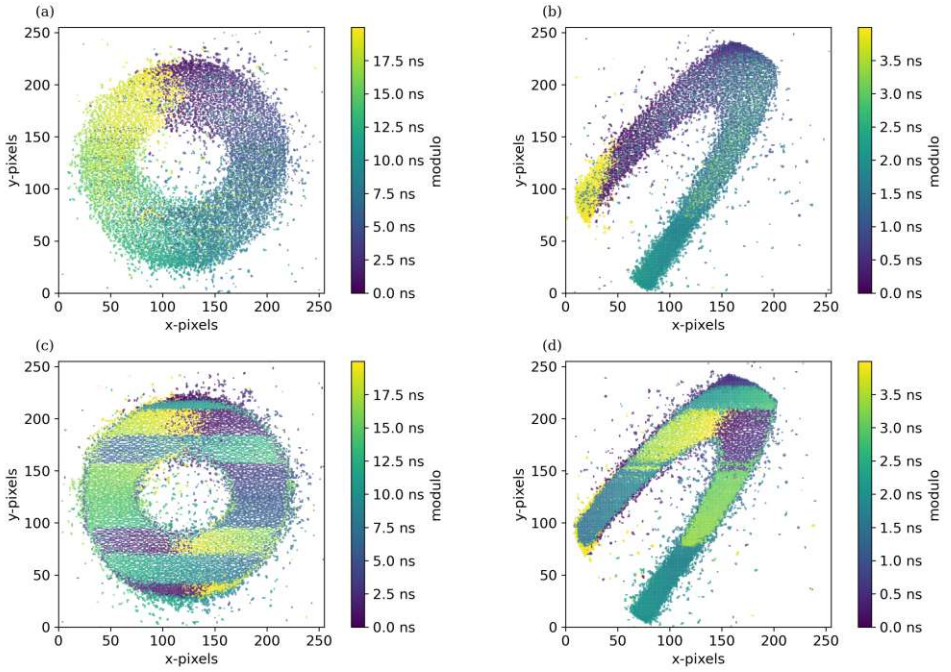

Figure 4.5: ToA stability analysis. 50/250 kHz modulus data in the beginning of the measurement (a/b), where the start of a period is visible by the border between yellow and purple, followed by shifted patterns (c/d).

signal [54]. This holder enables the deflection of the electron beam by applying microwave (MW) radiation. The result is an oscillating electron beam at the frequency of the MW generator. We use this modulated electron beam to assess whether the per-pixel time stamps align consistently with the modulation frequency.

Fig. 4.5 shows the temporal data of two modulation frequencies at 50 kHz and 250 kHz. The colours in the plots represent the modulus of the ToA value with respect to the modulation frequency. In the beginning of the data acquisition (Fig. 4.5a/b), the oscillating beam can be reconstructed with the correct periodicity, and the time stamps align with the modulated electron beam in this portion of the data set. However, after several cycles (Fig. 4.5c/d), distinct horizontal patterns occur. While the modulation shape is contained, it seems that in this particular case the time stamps of entire row patches are desynchronised or shifted. The pattern remains until the end, which might be an indication that an error happened in the read-out electronics.

In summary, the calibration technique presented in this section has proven to be an efficient method for testing temporal stability and allows us to compensate for apparent pixel clock deviations to achieve better temporal resolution.

5 Who kicked the electron?

Massive particles cannot exceed the speed of light in a vacuum. However, the speed of light can be reduced within a medium. This allows relativistic particles, such as a 200 keV electron, to travel faster than the phase velocity of light in that medium. One phenomenon that occurs under these conditions is the Cherenkov effect. If an electron travels through a medium faster than the phase velocity of light $v > c$, it can emit Cherenkov radiation. The emission pattern of the generated photons forms a radially symmetric cone, which appears as a ring shape when projected onto the xy plane. In this chapter, we investigate the diffraction pattern of a 100 nm silicon membrane. Fig. 5.1 presents a magnified energy-filtered image of the zero-order peak. Due to momentum conservation, a distribution resembling the Cherenkov cone is observed on the electron beam in EFTEM, achieved by energy filtering for energy losses in the optical range (1.55-4.13 eV for 300-800 nm from Eq. 3.2). This raises an important question: Are the electrons responsible for generating Cherenkov photons located on the ring? This question, along with the theoretical considerations of this experiment, has been explored in detail by A. Preimesberger et al. [31].

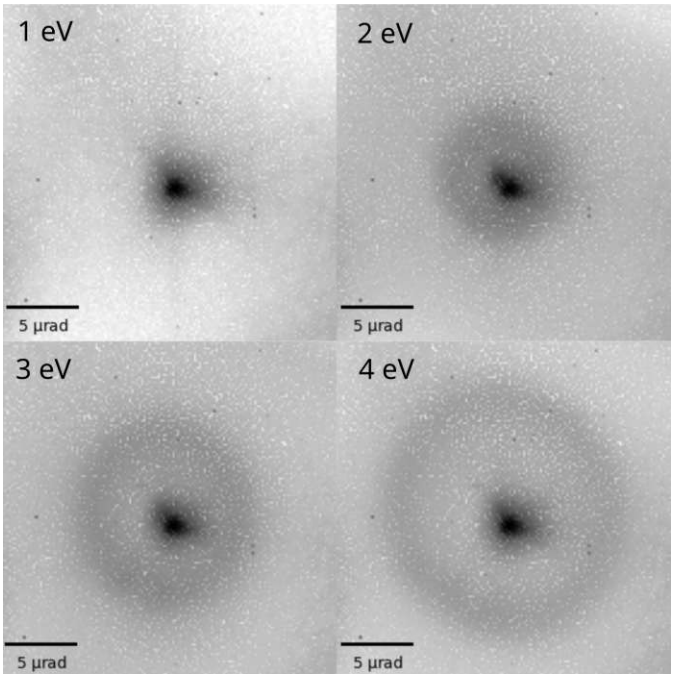

Figure 5.1: A magnified EFTEM image of the zero-order peak of the diffraction pattern from a 100 nm silicon membrane. The central bright spot corresponds to non-deflected electrons. A ring appears when the energy filter is set to select energy losses in the optical range (1.55-4.13 eV for 300-800 nm from Eq. 3.2). The radius of the ring increases with higher energy losses, potentially indicating that the emission of a higher-energy photon causes a greater recoil on the electron, consistent with energy and momentum conservation. The electron energy loss filter setting is marked in the top-left corner, with the slit width set to $\Delta E \pm 0.5$ eV.

5.1 Energy and Momentum Conservation

To understand how a photon is created in the Cherenkov effect, we begin with energy/momentum conservation:

$$p_a^\mu = p_e^\mu + p_\gamma^\mu \tag{5.1}$$

p_a^μ is the four-momentum of the electron before the interaction and p_e^μ after the emission of a photon with the momentum p_γ^μ. In the following, we assume that no momentum is transferred to the medium. The electron enters the material with energy E_a and momentum $\vec{p_a}$. After emission of a photon $E_\gamma = h\nu$ with momentum $\vec{p_\gamma} = \hbar\vec{k}$, the electron energy is reduced by $E_e = E_a - h\nu$ and is deflected due to momentum conservation by $\vec{p_e} = \vec{p_a} - \hbar\vec{k}$. This results in two conditions:

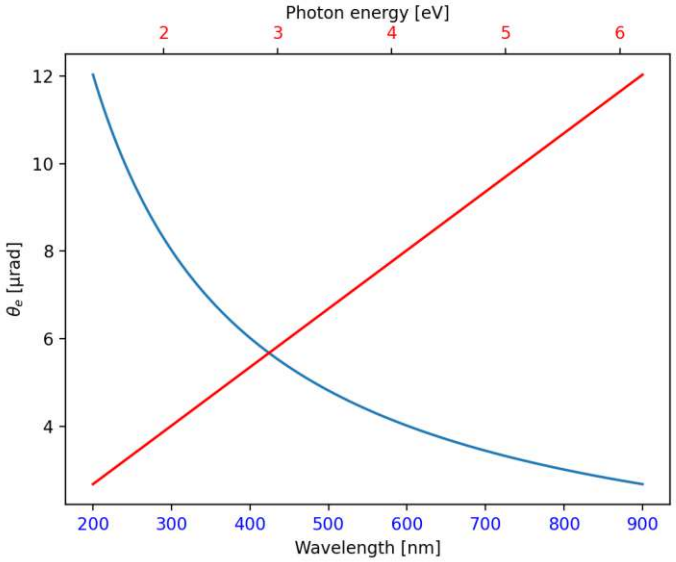

Figure 5.2: Electron deflection angle as a function of wavelength and photon energy.

$$E_a = E_e + E_\gamma \tag{5.2}$$

$$\vec{p}_a = \vec{p}_e + \vec{p}_\gamma \tag{5.3}$$

We assume radial symmetry and calculate how much the electron is deflected (y-axis) from its initial trajectory (x-axis) after the interaction:

$$\begin{pmatrix} x \\ y \end{pmatrix} = \begin{pmatrix} |\vec{p}_a| \\ 0 \end{pmatrix} = \begin{pmatrix} |\vec{p}_a| \cos\theta_e \\ |\vec{p}_a| \sin\theta_e \end{pmatrix} + \begin{pmatrix} \hbar|\vec{k}| \cos\theta_{ph} \\ -\hbar|\vec{k}| \sin\theta_{ph} \end{pmatrix} \tag{5.4}$$

Solving for $|\vec{p}_a|$ in the y-component, inserting it on the right side of the x-component in Eq. 5.4 and approximating $\tan\theta_e \approx \theta_e$, we get

$$\theta_e = \frac{\hbar|\vec{k}| \sin\theta_{ph}}{|\vec{p}_a| - \hbar|\vec{k}| \cos\theta_{ph}} \tag{5.5}$$

We see that the deflection of the electron depends on its initial momentum $|\vec{p}_a|$, the photon momentum $|\vec{p}_\gamma| = \hbar|\vec{k}| = \hbar\frac{2\pi}{\lambda_\gamma}$ and the photon emission angle θ_{ph}. If we insert the Cherenkov angle $\theta_{\text{Ch}} = 69°$ (n ≈ 3.8 for silicon, $\beta = 0.7$ for 200 keV electron) for θ_{ph}, the electron deflection angle ranges from 3-12 µrad for λ_γ =200-900 nm (1.38-6.2 eV) photons, shown in Fig. 5.2. This approximately fits the deflection angles seen in the electron deflection distribution from Fig. 5.1.

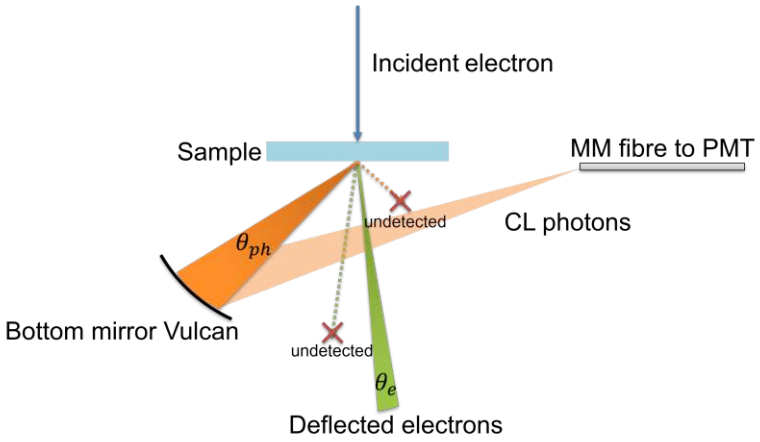

Figure 5.3: Schematic of CL collection within the Gatan Vulcan holder. CL photons are reflected by elliptical mirrors into multi-mode fibres for detection. Photons that miss the mirror are not guided into the fibre and therefore cannot be detected in coincidence with the corresponding incident electron.

5.2 Ghost Imaging

To understand the images formed by correlated electron-photon pairs, it is helpful to consider the concept of ghost imaging. This technique reconstructs an image by correlating signals from two detectors: a spatially resolved multi-pixel detector (such as TP3) and a non-imaging single-pixel detector (such as an SPCM). Both detectors are illuminated by the same light source, while an object is placed only in the path of the single-photon detector. The key idea behind ghost imaging is that even though the single-pixel detector does not provide any spatial information, the image can still be reconstructed by statistical correlations with the spatially resolved detector. The photon beam interacting with the object carries no spatial information, but it shares quantum and classical correlations with the photons detected by the multi-pixel detector. Over many coincidence events, a full image can be reconstructed, hence the term "ghost" imaging.

In our case, the illumination source is coherent CL and the electron-photon pairs are not only temporally correlated but also exhibit correlations in momentum. The TP3 serves as our multi-pixel electron detector, while the photons are detected with an SPCM, acting as the non-imaging detector. Even though the photon path carries no spatial resolution, we can reconstruct the spatial information from the photon path on the electron side. This forms the basis of ghost-imaging in transmission electron microscopy, enabling us to study fundamental scattering mechanisms and their underlying process.

Our setup uses a 100 nm silicon membrane provided by Silson [55] placed inside

the Gatan Vulcan holder. The specimen is illuminated by a collimated electron beam, the CL photons are collected from the bottom elliptical mirror and detected by a PicoQuant PMT. The electron beam is operated at 200 kV with a current of 3 pA, corresponding to $\approx 18 \cdot 10^6\, e^-/s$. The schematic of the setup is shown in Fig. 5.3. In this configuration, the photon emission causes the electron to recoil in the opposite direction, resulting in a deflection that leads to an anti-correlation in transverse momentum between electron and the emitted photon, described by $p_{e_\perp} = -p_{\gamma_\perp}$. The coherent CL signal that we detect is primarily attributed to transition radiation emitted on the bottom boundary between the membrane and vacuum. This occurs because the silicon membrane acts as a waveguide, effectively confining Cherenkov photons inside the medium. However, the energy and momentum conservation principles associated with transition radiation remain valid, meaning the initial electron still undergoes a corresponding energy loss and momentum recoil.

Fig. 5.4 presents the results of several coincidence measurements, illustrating how ghost images evolve under electron and photon filtering. We begin by evaluating the temporal cross-correlations using the BTH shown in Fig. 5.4a,d and g. Coincidences are counted per pixel within a coincidence window $-50\,\text{ns} < \Delta t < 50\,\text{ns}$ (coloured shaded area), which we define as the coincidence signal. Background coincidences are estimated from the interval $-250\,\text{ns} < \Delta t < -150\,\text{ns}$ (green shaded area) and subtracted from the coincidence signal. The resulting ghost images are shown in Fig. 5.4b,e and h with the corresponding radial intensity profiles displayed in Fig. 5.4c,f and i.

An interesting observation is that the intensity of the central spot in the raw data, visible as the dark region in Fig. 5.4b, decreases significantly after subtracting the background from the coincidence signal, displayed in Fig. 5.4c. This suggests that the background is dominated by random coincidences between undeflected electrons and uncorrelated photons, which can be effectively eliminated through background subtraction.

The ghost images seen in Fig.5.4b, e, and h resemble a horse-shoe pattern, which is exactly an image of the elliptical bottom mirror of the Gatan Vulcan holder, shown in Fig.3.3c. This pattern emerges due to the fact that the photons, primarily emitted from transition radiation, are reflected by the elliptical bottom mirror before being detected by the photon detector. The shape of the ghost image is directly related to the geometry of the mirror, as the photons follow distinct trajectories dictated by the mirror's curvature. This result emphasises the momentum correlation between the emitted photons and the electron beam, further confirming the coupling between electron trajectory and the emitted CL photons.

The setup allows for the application of both energy and photon filtering, enabling

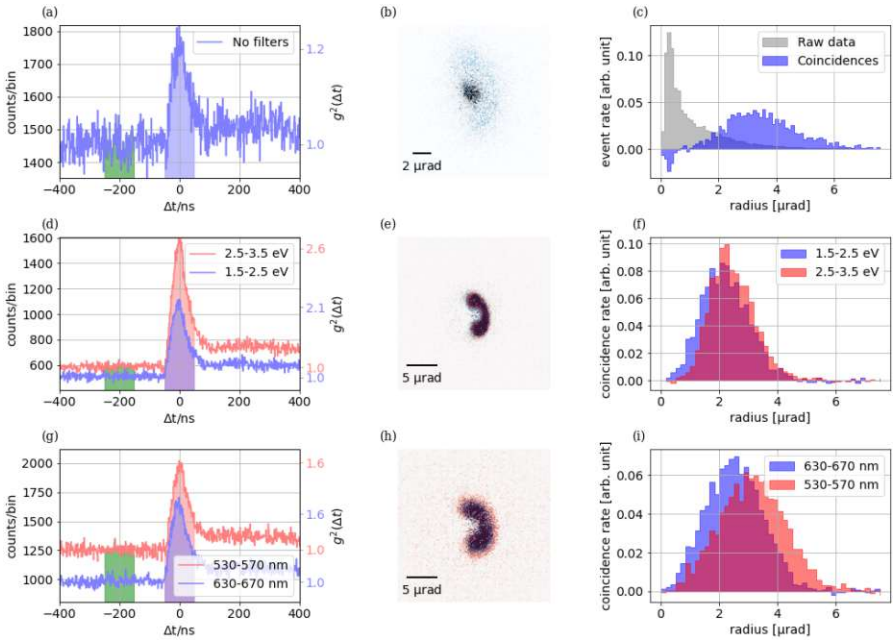

Figure 5.4: Coincidence measurements with a silicon membrane. (a) Bidirectional Temporal Histogram (BTH) of electron-photon pairs without energy filtering. (d) BTH with an electron energy slit applied. (g) BTH with optical bandpass filters and no electron filtering. The red and blue shaded areas correspond to the coincidence signal and the green shaded area to the background signal. (b) Intensity distribution of the unfiltered central spot (gray) compared to coincidence electrons (blue). The horse-shoe pattern becomes more distinct when energy filtering is applied to either the electrons (e) or the photons (h). (c,f,i) In a radial profile, coincidence electrons can be well distinguished from the central spot.

us to observe the impact of energy filtering on the ghost image. The contrast of the ghost images is quantified by the $g^2(\Delta t)$ value. Without energy filtering, the maximum g^2 value, approximately 1.2, as shown in Fig. 5.4a, is small, though a ghost image remains visible in Fig. 5.4b. The g^2 value increases significantly when either an electron filter (Fig. 5.4d) or an photon filter (Fig. 5.4g) is applied, enhancing the clarity of the ghost images in Fig. 5.4e and h. Additionally, a radial shift is observed in the radial profiles in Fig. 5.4f and i, highlighting that higher-energy photons induce a greater recoil on the electrons.

In summary, this experiment has demonstrated the potential of ghost imaging in revealing novel insights into electron-photon interactions. Further improvements in filtering and detection methods will allow for advanced explorations of the quantum properties of the systems under investigation.

6 Why do diamonds glow?

Diamonds are a fascinating material made up of carbon atoms arranged in a crystal structure. Not only are they a symbol of wealth and controversy, they can also glow in various colours when placed under an ultraviolet lamp. This fluorescence light is caused by lattice defects [56], which modify the electronic potential in such a way that an energy transition from a ground state to an excited state is possible.

In this experiment, we study incoherent CL from silicon defects in micro-diamonds called silicon vacancy centres (SiV). By inserting a wavelength bandpass filter in the optical path, we can isolate the spectral line of the characteristic transition and search for specific electron-photon correlations.

6.1 Vacancy Centres

Under high pressure and temperature, carbon atoms arrange themselves in a diamond cubic structure with all valence electrons creating covalent bonds. Single defects in the lattice can drastically change the electronic properties of the crystal matrix. A special type of defect that has been actively researched for the last years is the vacancy centre. A vacancy is formed when an impurity atom substitutes for one or more carbon atoms in the lattice, causing localised defects in the atomic arrangement. This defect exhibits a ground state and an excited electronic state, separated by an energy gap in the optical range. The system behaves like a two-level quantum system, where relaxation from the excited state to the ground state can occur through a purely electronic transition, without involving phonons or transferring momentum to the lattice. This process is associated with the zero-phonon line (ZPL) [57]. As a result, the vacancy centre itself can be seen as an artificial atom embedded in a diamond. In addition, because C^{12} atoms have no nuclear spin, the surrounding lattice introduces a minimal amount of magnetic noise, allowing the electron spin of the vacancy centre to act as a controllable degree of freedom. These properties make vacancy centres attractive candidates for quantum computing [58], quantum sensors [59], and as single-photon sources [60]. The most common naturally occurring vacancy defects are nitrogen vacancy centres. They can be either in a neutral charge state (NV^0) with a ZPL at 575 nm or in a negative charge state (NV^-) at 637 nm [61]. The emission spectrum of both types of NV centre is broad at room temperature, which increases the difficulty of

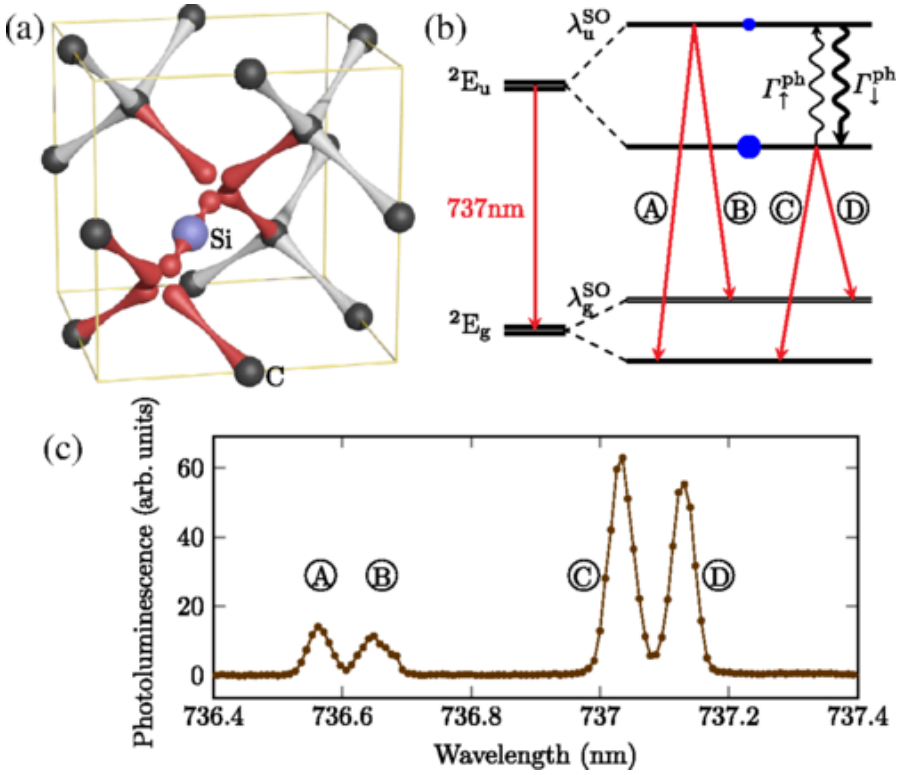

Figure 6.1: Silicon vacancy structure in diamond. (a) Crystal structure of a silicon vacancy. (b) Optical transition at 737 nm and Zeeman splitting. (c) The emission spectrum at 4.5K. The figure has been adopted from [63]

isolating the ZPL with bandpass filters.

Another element that can form vacancy structures is silicon, shown in Fig.6.1a, where the silicon atom places itself between two vacancies. This means that the fluorescence will primarily be radiated in a dipole-like radiation pattern [62], which results in an orientation-dependent intensity distribution. The main electronic transition of interest is the photon emission line at 737 nm (1.68 eV)(Fig. 6.1b). The full spectral Zeeman splitting of the ZPL is visible only at cryogenic temperatures (Fig. 6.1c).

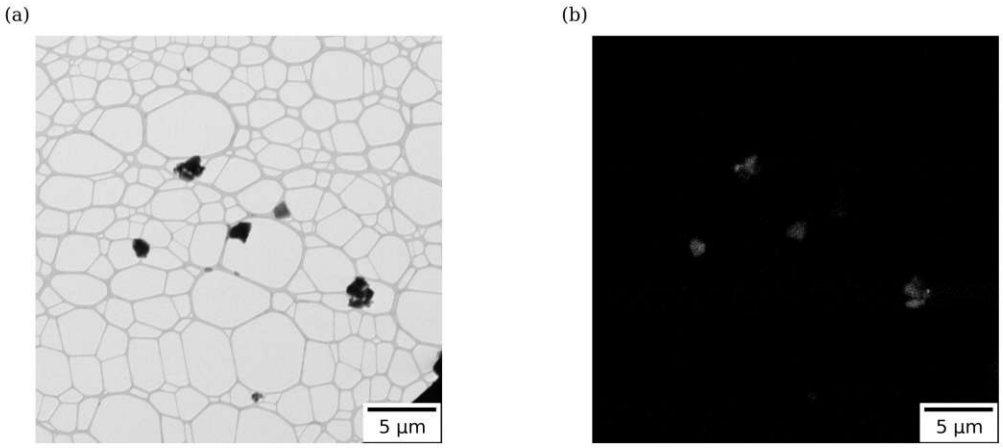

Figure 6.2: (a) STEM bright field image of a silicon vacancy sample on a lacey carbon grid. (b) A CL photon count map shows bright crystals.

6.2 STEM CL

Before acquiring coincidence data, we must prepare a sample for CL measurements, characterise the CL emission spectrum and identify suitable crystals for further investigations. The first step is to analyse the CL spectrum of the SiV crystals, produced by Adamas nano [64], in a TEM. The container with the SiV crystals in water is held in an ultrasonic bath to separate clustered micro-diamonds. Afterwards, the SiV crystals are transferred from the container onto a 200 lacey carbon copper mesh grid [65] using a Pasteur pipette. As soon as all liquids have evaporated, we place the grid in the Vulcan holder and analyse the result using STEM CL within an FEI Tecnai F20 TEM.

Fig. 6.2a shows a typical SiV sample. The diamonds are well separated, and some crystal edges are inside the holes of the lacey carbon films. This is beneficial when we try to perform EELS measurements without the influence of the carbon support layer. An overview picture of the photon counts per pixel reveals bright diamonds, see Fig. 6.2b. It speeds up the search for crystals that are bright enough for subsequent measurements.

Next, we analyse the spectral emission distribution of a small SiV crystal, as seen in Fig. 6.3a. For that we record the CL emission along two line profiles, one vertical and one horizontal (Fig. 6.3b and c). The CL spectra show a strong signal between 730 and 740 nm wavelength, which fits the 737 nm ZPL from the SiV centres.

A comparison between wavelength regions below 700 nm and the ZPL range between 730 and 780 nm, as shown in Fig. 6.3d and e, reveals that the emission from the SiV centres is more intense within the ZPL region. This suggests that

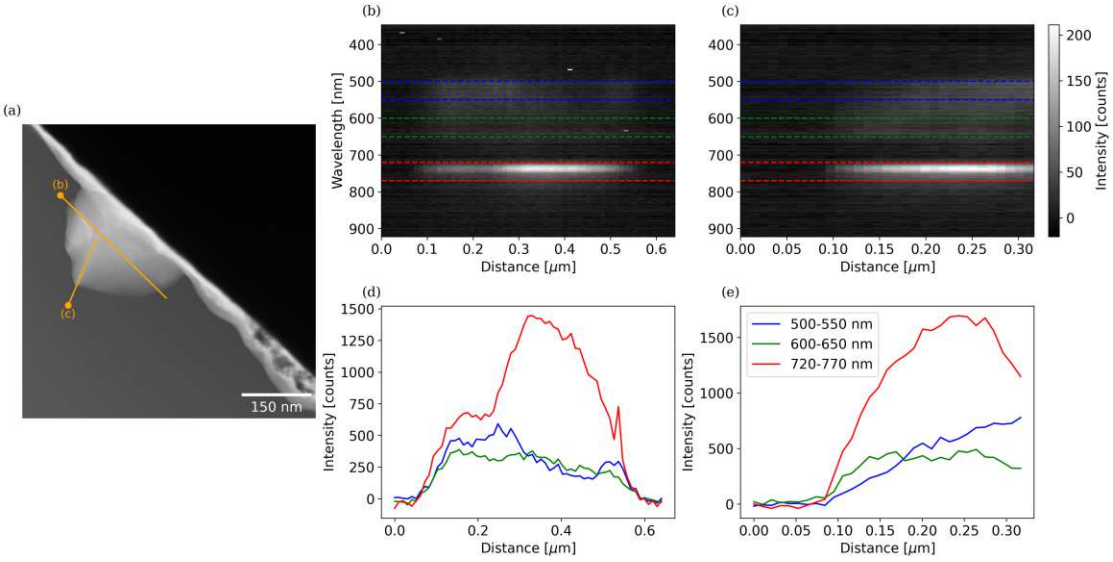

Figure 6.3: Spectral imaging of a small SiV crystal. (a) Overview STEM image of an SiV nanodiamond. The lines are indicate the positions of a vertical (b) and a horizontal (c) CL line spectrum. The points of each line mark the beginning of the line profiles. (d,e) Intensity profiles corresponding to different wavelength ranges, obtained by integrating over a 50 nm spectral window.

isolating the ZPL with a photon filter could enable the detection of coincidence signals by suppressing background CL not associated with the ZPL emission.

6.3 Coincidence EELS

In the previous measurement, we gained insight into the CL spectrum emitted by SiV centres irradiated by an electron beam. Building on these findings, we now aim to correlate the excitation of the ZPL by acquiring the CL photons in coincidence with the EELS spectrum.

Fig. 6.4 illustrates how the EELS spectrum of a SiV crystal changes when filtered for coincidence electrons. A focused 200 keV electron beam is placed on the crystal border (red circle in Fig. 6.4a) and the EELS spectrum of the transmitted electrons is recorded simultaneously with the unfiltered CL photons. The temporal cross-correlation histogram in Fig. 6.4d shows a peak g^2 value of 1.3 at an 58.3 ns offset. By fitting a Lorentzian curve to this peak, we obtain a median absolute deviation of $\gamma = 19.3$ ns. Therefore, we define the total temporal uncertainty as $\delta t = 58.3 \pm 19.3$, which we define as the coincidence window for our coincidence signal (orange area). The background signal is estimated at $\delta t - 400\,\text{ns}$. The raw signal of the EELS data (blue area) is plotted in Fig. 6.4b. If we now only consider

electron-photon coincidences inside the window of $g^2(\delta t)$ (Fig. 6.4d), we obtain the coincidence EELS spectrum (CEELS), seen in Fig. 6.4c. The CEELS spectrum shows two peaks at $\Delta E = 0$ eV and a second peak at $\Delta E = 1.75$ eV. We continue the investigation of these features by applying a background subtraction to the coincidence signal.

Fig. 6.5a shows the CEELS spectrum of the background signal at a time offset $\delta t - 400\,\text{ns}$, which is then subtracted from the spectrum presented in Fig. 6.4c. The resulting corrected spectrum is shown in Fig. 6.5b. The intensity of the zero-loss peak at $\Delta E = 0$ eV decreases significantly while the peak at $\Delta E = 1.75$ eV (≈ 710 nm from Eq. 3.2) remains. This feature may arise either from a direct excitation of the ZPL, as shown in Fig. 3.5d, or from coherent CL predominantly emitting photons around 1.75 eV. We may rule out indirect excitations of the ZPL (Fig. 3.5e) as they involve the generation of a mediator particle, which typically leads to greater electron energy losses than the ZPL.

By correlating CL photon emission with EELS signals, we have seen a clear enhancement of the feature at 1.75 eV that is not present without coincidence filtering. Although this feature aligns with the ZPL of the SiV centre, its exact origin remains uncertain and warrants further investigation.

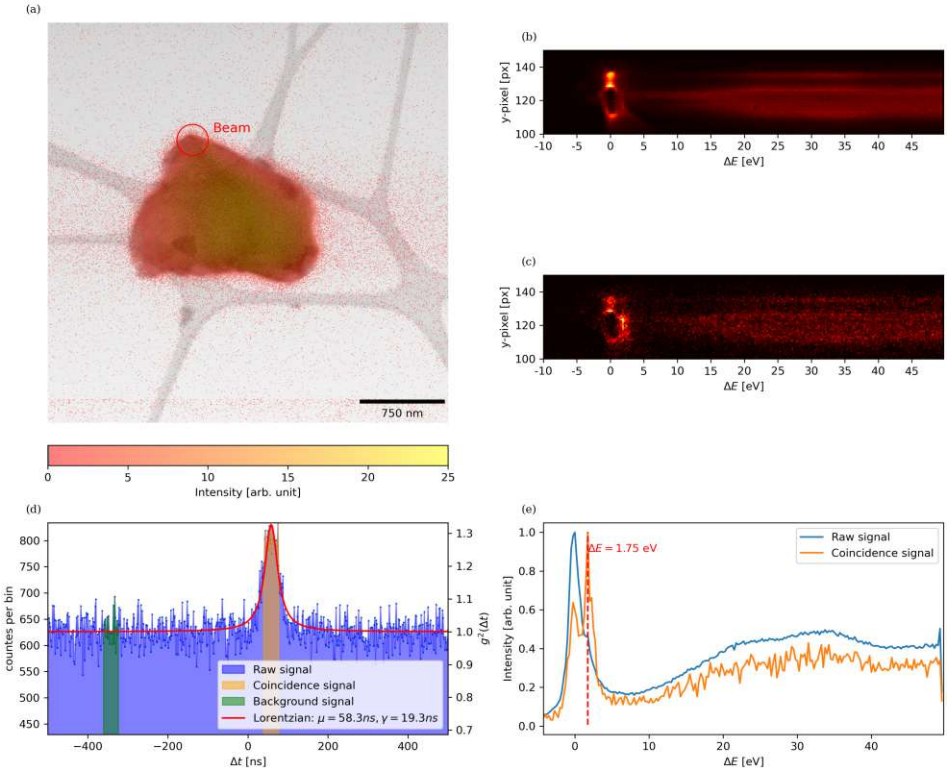

Figure 6.4: Coincidence EELS analysis of a SiV crystal. (a) Overview STEM picture superimposed with a CL intensity map. The red circle marks the position of the focused beam from which the coincidence EELS data were taken from. (b) Raw EELS image. (c) Coincidence EELS image from $g^2(\delta t)$. (d) Bidirectional temporal histogram fitted with a Lorentzian. The peak coincidence value at $\mu = 58.3$ ns and the median absolute deviation of $\gamma = 19.3$ ns sets our total temporal uncertainty to $\delta t = 58.3 \pm 19.3$ ns. (e) Coincidence EELS spectrum of (b) and (c) respectively.

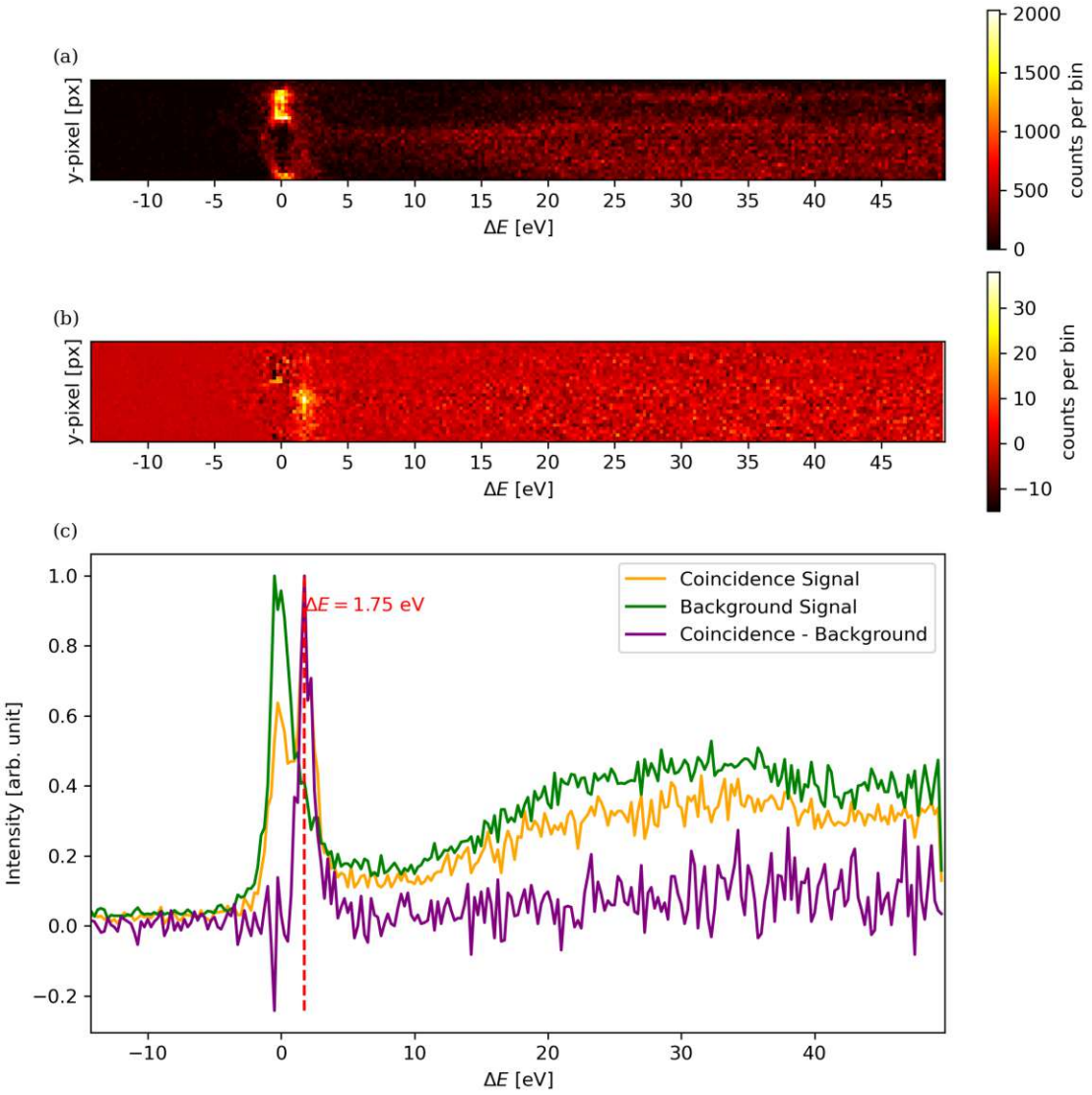

Figure 6.5: Background subtraction in CEELS. (a) EELS spectrum of the background signal recorded outside of the coincidence window. (b) Background-subtracted EELS spectrum showing the isolated coincidence signal. (c) Overlay of the coincidence spectrum, background spectrum, and their difference for comparison.

6.4 Coincidence EFTEM

In this section, we want to apply coincidence filtering for EFTEM imaging. A collimated beam illuminates two regions at the edge of the crystal displayed in Fig. 6.6a and we correlate the resulting EFTEM image with energy-filtered CL photons (750 ± 40 nm). The goal is to localise regions where electrons transmit through the crystal after emitting a photon that matches the ZPL at 737 nm of the SiV centres. To account for both direct and indirect excitation pathways, we apply a broad electron energy-loss filter covering the 1-50 eV range.

The results are shown in Fig. 6.6b-e. The histograms indicate a low coincidence rate, and it remains unclear whether a distinct coincidence signal is present. The energy filtered images in Fig. 6.6b and d suggest that the crystal is too thick in regions with a higher SiV centre density, displayed as the yellowish regions in Fig. 6.6a, preventing sufficient electron transmission for coincidence detection. This highlights the challenge of detecting a coincidence signal in thicker regions of the crystal, where electron transmission is limited. To improve the signal-to-noise ratio, we could find thinner crystals or cool down the specimen.

6.5 Cryo CL

The previous section showed that SiV crystals exhibit reduced coincidence performance at room temperature. To enhance the signal-to-noise ration, we cool the specimen using liquid nitrogen (LN), which should improve the measurement conditions.

Fig. 6.7 presents the CL spectrum of cold SiV crystals. The electron beam is placed on two different crystals (Fig. 6.7a and b) and a high-resolution CL spectrum is recorded at room temperature (296 K $\approx$ 23°C) and at 213 K ($\approx$ -60°C). The spectra in Fig. 6.7c and d have been normalised so that the maximum is equal to one in order to compare the shape of the ZPL, which is noticably narrower at cold temperatures. Unfortunately, coincidence measurements were not possible due to sample drifts caused by temperature instability ($\approx$50 nm/min) of the CL holder (Fig. 6.8). Future experiments could investigate thin SiV centres at cryogenic temperatures below 100 K. This would allow for the repetition of the experiments presented in this chapter, taking advantage of the enhanced signal-to-noise ratio that cooling provides.

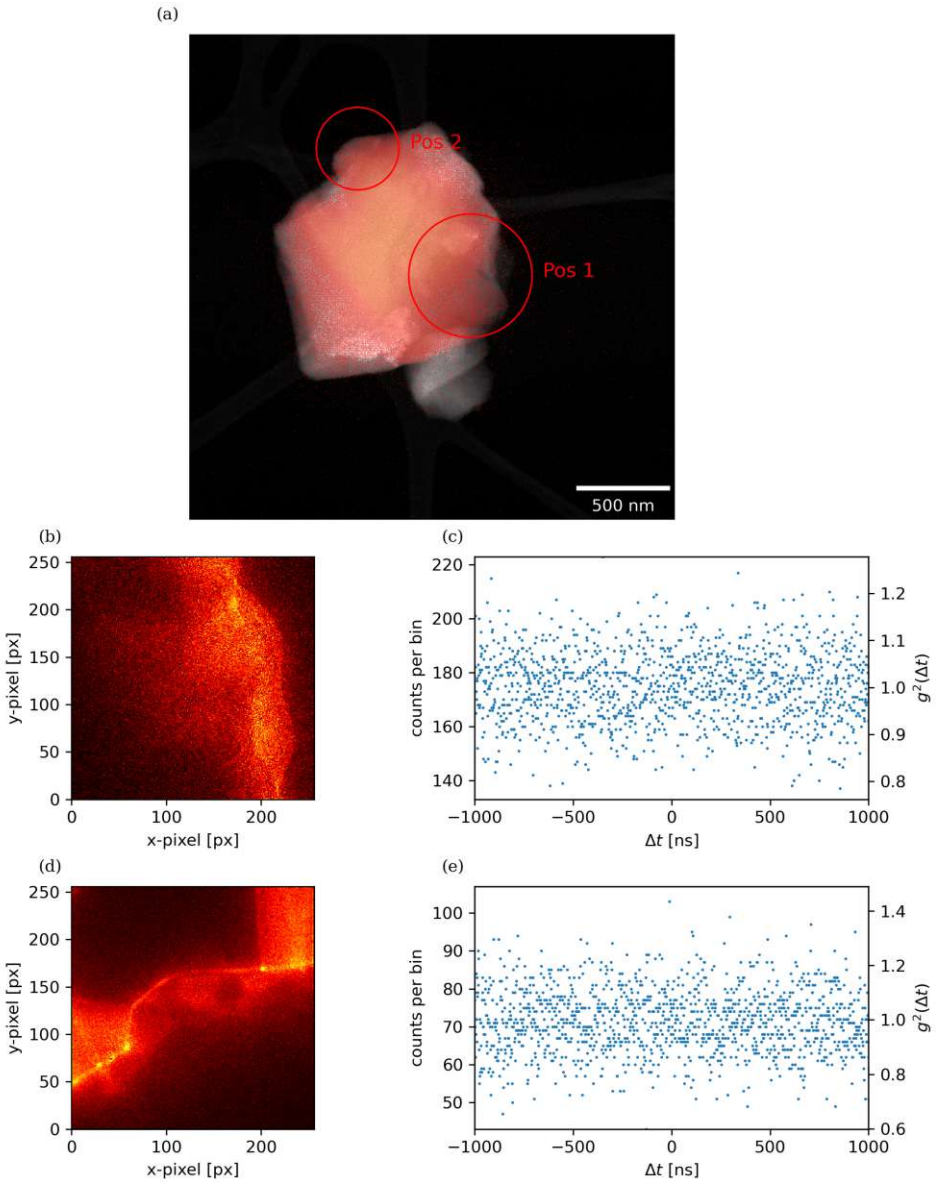

Figure 6.6: Coincidence EFTEM results on a big SiV crystal. (a) Overview picture with a CL intensity map (red-yellow) superimposed. The red circles highlight the area illuminated by the collimated beam. (b,d) EFTEM images of Position 1 and 2, respectively, with an energy-loss filter setting of 1-50 eV, specifically filtering out the zero-loss electrons. We can observe that electrons only transmit through the thinner regions of the crystal, while the thicker regions remain dark. (c,e) Bidirectional temporal histogram of Position 1 and 2, recorded with a 750 ± 40 nm bandpass filter. In this configuration, electrons in the EFTEM images are temporally correlated with photon energies corresponding to the ZPL of the SiV centers.

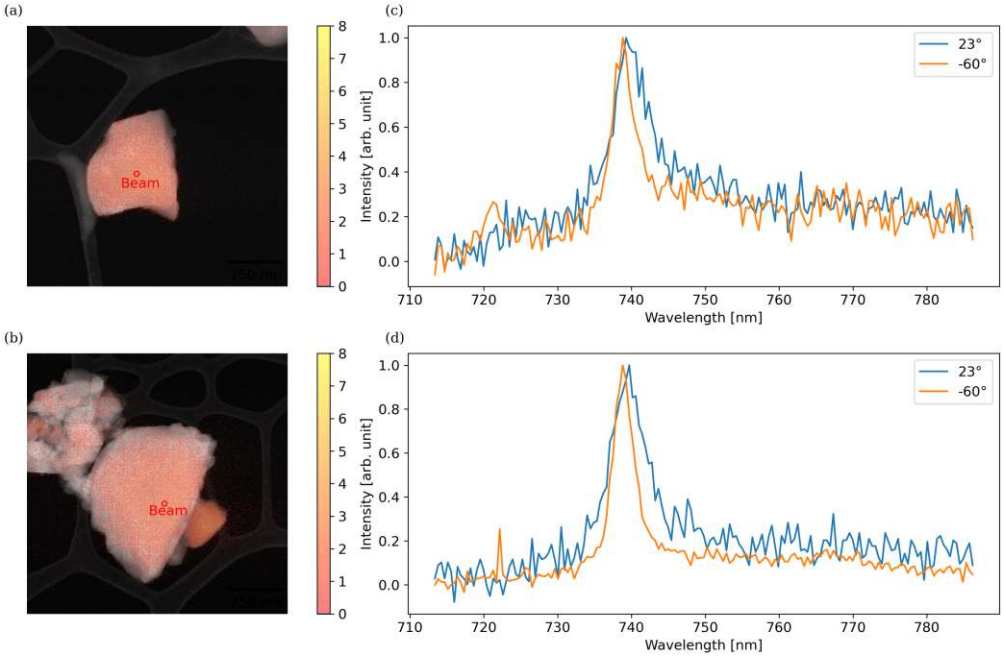

Figure 6.7: Cryo CL measurements. (a,b) Overview STEM dark field pictures of two different crystals superimposed with a CL intensity map (red-yellow). (c,d) High resolution CL spectrum of (a) and (b), respectively. The ZPL becomes noticeably narrower at low temperatures.

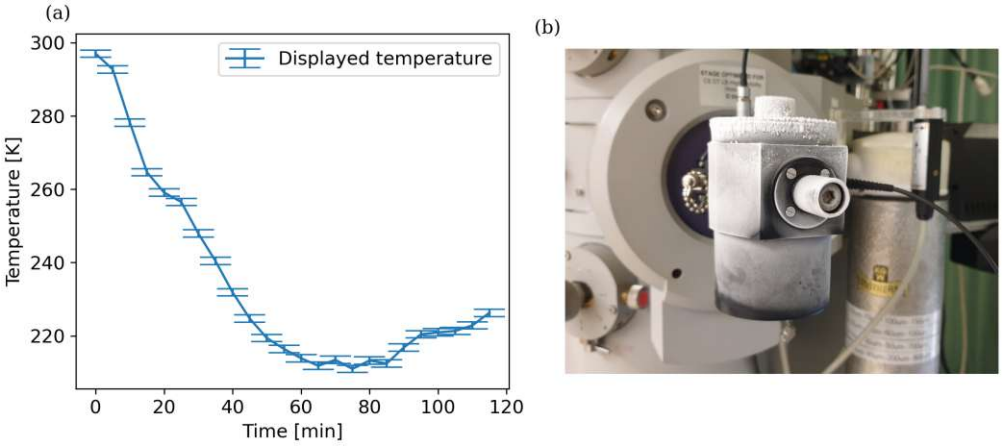

Figure 6.8: (a) Temperature curve over time of the Gatan Vulcan holder during cooling with liquid nitrogen. (b) Gatan Vulcan holder after 120 minutes cooling. The presence of ice crystals forming on the outside of the dewar suggests that the vacuum seal is insufficient, allowing heat to enter and compromising the ability to sustain cryogenic temperatures.

7 Discussion

Coincidence microscopy using electron photon correlations is a powerful method for investigating fundamental excitation and scattering processes. In this work, we applied this technique to study artifical atoms, such as SIV centers, revealing information that is otherwise obscured by incoherent processes and background signals.

Calibrating the time resolved electron camera, Timepix3, is a critical step in achieving more precise coincidence measurements. We developed a method that characterises the timing precision of TP3 without requiring temporal electron-photon coincidences, providing a significant advantage in terms of calibration efficiency. With this enhanced temporal resolution, we were able to directly observe the momentum recoil of an electron resulting from the emission of a single photon in the diffraction pattern. The evolution of the ghost images, as shown by various filtering conditions, underscores the ability to probe and refine our understanding of the fundamental processes occurring during electron-matter interactions.

Furthermore, by adjusting the microscope lens settings, we can transition from imaging momentum (via diffraction patterns) to spatial imaging, enabling us to reconstruct the position where photon emission events occurred. This ability to measure both spatial and momentum correlations between the electron and the emitted photon in a controlled way opens the door to certifying entanglement in coherent cathodoluminescence processes [66].

The entanglement of electron-photon pairs opens the door to advanced quantum optic schemes in electron microscopy. Established photonic quantum optic techniques with entangled photon pairs [67, 68] could be easily adapted to electron microscopy, combining the subatomic resolution of the electron microscope with the highly controllable photons.

In conclusion, further advancements in coincidence microscopy will provide deeper insights into the optical transition properties of artificial atoms, including excitation pathways and coherence times. These improvements hold the potential to accelerate the development of quantum memory technologies and open up new possibilities for quantum-enhanced imaging techniques in transmission electron microscopy.

Bibliography

1. Robinson, B. L. & Madansky, L. Coincidence Studies in the Decay of La 140. *Phys. Rev.* **84,** 1067–1068 (1951).
2. Bennink, R. S., Bentley, S. J., Boyd, R. W. & Howell, J. C. Quantum and Classical Coincidence Imaging. *Phys. Rev. Lett.* **92,** 033601 (2004).
3. Keevend, K., Coenen, T. & Herrmann, I. K. Correlative cathodoluminescence electron microscopy bioimaging: towards single protein labelling with ultrastructural context. *Nanoscale* **12,** 15588–15603 (2020).
4. Dierre, B., Yuan, X. & Sekiguchi, T. Low-energy cathodoluminescence microscopy for the characterization of nanostructures. *Science and Technology of Advanced Materials* **11,** 043001 (2010).
5. Abbe Hon., E. VII.—On the Estimation of Aperture in the Microscope. *Journal of the Royal Microscopical Society* **1,** 388–423 (1881).
6. Knoll, M. & Ruska, E. Das Elektronenmikroskop. *Zeitschrift für physik* **78,** 318–339 (1932).
7. Chen, Z. *et al.* Electron ptychography achieves atomic-resolution limits set by lattice vibrations. *Science* **372,** 826–831 (2021).
8. Carter, C. B. & Williams, D. B. *Transmission Electron Microscopy: Diffraction, Imaging and Spectrometry* (Springer, 2016).
9. Young, T. II. The Bakerian Lecture. On the theory of light and colours. *Philosophical transactions of the Royal Society of London,* 12–48 (1802).
10. Crookes, W. On radiant matter. *American Journal of Science* **3,** 241–262 (1879).
11. Davisson, C. & Germer, L. H. The scattering of electrons by a single crystal of nickel. *Nature* **119,** 558–560 (1927).
12. Planck, M. in *Von Kirchhoff bis Planck: Theorie der Wärmestrahlung in historisch-kritischer Darstellung* 178–191 (1978).
13. De Broglie, L. Waves and quanta. *Nature* **112,** 540–540 (1923).
14. Schrödinger, E. Quantisierung als Eigenwertproblem. *Annalen der Physik* **386,** 109–139 (1926).

15. USTEM. TECNAI G20 "ultra low voltage". https://www.tuwien.at/forschung/facilities/ustem/geraeteausstattung/tecnai-g20 (2023).

16. Potapov, P. The experimental electron mean-free-path in Si under typical (S)TEM conditions. *Ultramicroscopy* **147,** 21–24 (2014).

17. Puluj, J. Strahlende Elektrodenmaterie. *Repertorium für Experimental-Physik, für physikalische Technik, mathematische und astronomische Instrumentenkunde* **17,** 69 (1881).

18. Crookes, W. A Fourth State of Matter. *Science,* 32–33 (1880).

19. García de Abajo, F. J. Optical excitations in electron microscopy. *Reviews of modern physics* **82,** 209–275 (2010).

20. Bothe, W. & Geiger, H. Über das Wesen des Comptoneffekts; ein experimenteller Beitrag zur Theorie der Strahlung. *Zeitschrift für Physik* **32,** 639–663 (1925).

21. Einstein, A., Podolsky, B. & Rosen, N. Can quantum-mechanical description of physical reality be considered complete? *Physical review* **47,** 777 (1935).

22. Bell, J. S. On the Einstein Podolsky Rosen paradox. *Physics Physique Fizika* **1,** 195–200 (1964).

23. Clauser, J. F., Horne, M. A., Shimony, A. & Holt, R. A. Proposed Experiment to Test Local Hidden-Variable Theories. *Phys. Rev. Lett.* **23,** 880–884 (1969).

24. Aspect, A., Grangier, P. & Roger, G. Experimental tests of realistic local theories via Bell's theorem. *Physical review letters* **47,** 460 (1981).

25. Hensen, B. *et al.* Loophole-free Bell inequality violation using electron spins separated by 1.3 kilometres. *Nature* **526,** 682–686 (2015).

26. Giustina, M. *et al.* Significant-loophole-free test of Bell's theorem with entangled photons. *Physical review letters* **115,** 250401 (2015).

27. Glauber, R. J. The Quantum Theory of Optical Coherence. *Phys. Rev.* **130,** 2529–2539 (1963).

28. Yanagimoto, S., Yamamoto, N., Yuge, T., Sannomiya, T. & Akiba, K. Unveiling the nature of cathodoluminescence from photon statistics. *Communications Physics* **8,** 56 (2025).

29. Brown, R. H. & Twiss, R. Q. Correlation between Photons in two Coherent Beams of Light. *Nature* **177,** 27–29 (1956).

30. Yanagimoto, S. *et al.* Time-correlated electron and photon counting microscopy. *Communications Physics* **6,** 260 (2023).

31. Preimesberger, A. *et al.* Exploring Single-Photon Recoil on Free Electrons. *Phys. Rev. Lett.* **134,** 096901 (2025).

32. Preimesberger, A. *Identifying viable experimental configurations for the study of correlated electron-photon pairs in the transmission electron microscope* MA thesis (Technische Universität Wien, 2023).

33. Cerenkov, P. *et al.* Visible emission of clean liquids by action of γ radiation. *Dokl. Akad. Nauk SSSR* **2,** 451–454 (1934).

34. Goldsmith, P. & Jelley, J. Optical transition radiation from protons entering metal surfaces. *Philosophical Magazine* **4,** 836–844 (1959).

35. Smith, S. J. & Purcell, E. M. Visible Light from Localized Surface Charges Moving across a Grating. *Phys. Rev.* **92,** 1069–1069 (1953).

36. Solà-Garcia, M. *et al.* Photon statistics of incoherent cathodoluminescence with continuous and pulsed electron beams. *ACS photonics* **8,** 916–925 (2021).

37. Iyer, V. *et al.* Photon bunching in cathodoluminescence induced by indirect electron excitation. *Nanoscale* **15,** 9738–9744 (2023).

38. Schilder, N. J., Agrawal, H., Garnett, E. C. & Polman, A. Phase-resolved surface plasmon scattering probed by cathodoluminescence holography. *ACS photonics* **7,** 1476–1482 (2020).

39. Thorlabs. Spectral Filters. `https://www.thorlabs.com/navigation.cfm?guide_id=2210`.

40. Advascope. ePix TimePix 3. `https://advascope.cz/products/ePixTimepix3ext`.

41. Poikela, T. *et al.* Timepix3: a 65K channel hybrid pixel readout chip with simultaneous ToA/ToT and sparse readout. *Journal of instrumentation* **9,** C05013 (2014).

42. medipix collaboration. Medipix3. `https://medipix.web.cern.ch/medipix3`.

43. Swabian Instruments. Time Tagger Series. `https://www.swabianinstruments.com/time-tagger/`.

44. Advascope. Advascope SDK Manual. `https://advascope.gitlab.io/sdk/advssdkdocs/0.7.1/index.html` (2024).

45. Swabian Instruments. Time Tagger User Manual. `https://www.swabianinstruments.com/static/documentation/TimeTagger/index.html` (2025).

46. Excelitas. SPCM AQRH. `https://www.excelitas.com/product/spcm-aqrh`.

47. PicoQuant. PMA Hybrid Series. `https://www.picoquant.com/products/category/photon-counting-detectors/pma-hybrid-series-hybrid-photomultiplier-detector-assembly`.

48. Thorlabs. Multimode Fiber Optic Filter/Attenuator Mounts. `https://www.thorlabs.com/newgrouppage9.cfm?objectgroup_id=10066`.

49. Turecek, D., Jakubek, J. & Soukup, P. USB 3.0 readout and time-walk correction method for Timepix3 detector. *J. Inst.* **11,** C12065–C12065. (2025) (2016).

50. Pitters, F. *et al.* Time resolution studies of Timepix3 assemblies with thin silicon pixel sensors. *J. Inst.* **14,** P05022–P05022 (2019).

51. Auad, Y. *et al.* Time calibration studies for the Timepix3 hybrid pixel detector in electron microscopy. *Ultramicroscopy* **257,** 113889 (2024).

52. Ester, M., Kriegel, H. P., Sander, J. & Xu, X. A Density-Based Algorithm for Discovering Clusters in Large Spatial Databases with Noise. *Proceedings of the 2nd International Conference on Knowledge Discovery and Data Mining* (1996).

53. The Scipy community. scipy.optimize. curve_fit. `https://docs.scipy.org/doc/scipy/reference/generated/scipy.optimize.curve_fit.html`.

54. Jaroš, A. *et al.* Electron Spin Resonance Spectroscopy in a Transmission Electron Microscope. arXiv: `2408.16492` (2024).

55. Silson. Mono-crystalline (100) Silicon Membranes. `https://silson.com/product/silicon/`.

56. Jelezko, F. & Wrachtrup, J. Single defect centres in diamond: A review. *physica status solidi (a)* **203,** 3207–3225 (2006).

57. Bradac, C., Gao, W., Forneris, J., Trusheim, M. E. & Aharonovich, I. Quantum nanophotonics with group IV defects in diamond. *Nature communications* **10,** 5625 (2019).

58. Yang, W. L., Yin, Z. Q., Hu, Y., Feng, M. & Du, J. F. High-fidelity quantum memory using nitrogen-vacancy center ensemble for hybrid quantum computation. *Phys. Rev. A* **84,** 010301 (2011).

59. Bürgler, B. *et al.* All-optical nuclear quantum sensing using nitrogen-vacancy centers in diamond. *NPJ quantum information* **9,** 56 (2023).

60. Benedikter, J. *et al.* Cavity-Enhanced Single-Photon Source Based on the Silicon-Vacancy Center in Diamond. *Phys. Rev. Applied* **7,** 024031 (2017).

61. Berthel, M. *et al.* Photophysics of single nitrogen-vacancy centers in diamond nanocrystals. *Physical Review B* **91,** 035308 (2015).

62. Rogers, L. J. *et al.* Electronic structure of the negatively charged silicon-vacancy center in diamond. *Physical Review B* **89,** 235101 (2014).

63. Sipahigil, A. *et al.* Indistinguishable Photons from Separated Silicon-Vacancy Centers in Diamond. *Phys. Rev. Lett.* **113,** 113602 (2014).

64. Adamas nano. Fluorescent Microdiamonds. https://www.adamasnano.com/fluorescent-microdiamond-information.

65. Micro to Nano. EMR Lacey carbon TEM Support Films. https://www.microtonano.com/EMR-TEM-support-films-Lacey-carbon-support-films-for-TEM.php.

66. Rembold, P. *et al.* State-Agnostic Approach to Certifying Electron-Photon Entanglement in Electron Microscopy. arXiv: 2502.19536 (2025).

67. Barz, S., Cronenberg, G., Zeilinger, A. & Walther, P. Heralded generation of entangled photon pairs. *Nature photonics* **4,** 553–556 (2010).

68. Altewischer, E., Van Exter, M. & Woerdman, J. Plasmon-assisted transmission of entangled photons. *Nature* **418,** 304–306 (2002).

Acknowledgements

First, I want to thank Philipp Haslinger for his undisputed inspiration and expertise. I remember the times when he was my tutor in my first semester at TU Wien and stayed longer after the exercise answering my questions even if he was in a rush. Despite COVID forcing us to stay home in 2020, Philipp Haslinger has made an effort to motivate his students to continue. I also want to thank him for letting me participate in some of his side projects. They are an encouragement to think outside the box and to be open to new ideas.

A colleague with whom I have spent a lot of time is Alexander Preimesberger. The coincidence that both of us come from Upper Austria is almost ironic and made the lab time even more pleasant. I greatly appreciate him as a working colleague, as a Mensa connoisseur, and as a loyal friend.

Whenever I needed help or spare parts for the experimental setup, I could ask Thomas Schachinger. Even when times were busy, one could rely on him to get crucial tips which sometimes determined the success or failure of the measurements. I thank him for his help and for showing me how to tinker with microscopes.

A person I especially want to mention is Michael Stöger-Pollach. At a certain point in my master studies I almost quit. He spoke to me at a crucial moment and motivated me to continue. I deeply thank him for his efforts.

My gratitude goes out to the other members of USTEM and the Haslinger group. Their support, kindness and knowledge helped me a lot whenever I needed colleagues, information and instructions.

I would like to thank Offek Tziperman and Prof. Ido Kaminer from Technion, Israel Institute of Technology, for providing me a sample of silicon vacancy microdiamond crystals. At the time of this master thesis, Israel is in a war and has complicated the collaboration. I wish both scientists the best for now and the future, wishing that we could meet again in better circumstances.

I want to mention Florian Michael Pitters who wrote a dissertation on the detector technology of TP3. The detailed explanations helped me a lot in understanding the working principle of TP3 and developing the methods of the calibration routine to our setup.

I thank Isobel Claire Bicket and Antonin Jaros, respectively postdoc and PhD student in the research group of Philipp Haslinger, for acquiring the modulated electron beam data with me, and Theo Dorfner who coded the algorithm that identified clustered events with `DBSCAN` to implement in the calibration routine.

Last but not least, I want to express my sincere thanks to my family and friends, who showed unwavering support and encouragement throughout my academic journey.